JGR Solid Earth

RESEARCH ARTICLE
10.1029/2022JB025253

Special Section:
Heterogeneity, anisotropy and scale-dependency: Keys to understand Earth composition, structure and behavior

Stress Effects on Wave Velocities of Rocks: Contribution of Crack Closure, Squirt Flow and Acoustoelasticity

Yijun Wei[1], Jing Ba[1], and José M. Carcione[1,2]

[1]School of Earth Sciences and Engineering, Hohai University, Nanjing, China, [2]National Institute of Oceanography and Applied Geophysics—OGS, Trieste, Italy

Abstract The elastic properties of rocks depend on the mineral constituents, pore structure, saturating fluids, and stress (loading) conditions. To study these properties, we measured ultrasonic P- and S-wave velocities as a function of the differential (confining minus pore) pressure and propose an unrelaxed double-porosity acoustoelasticity model, which generalizes the single-porosity one. The new approach includes the effects of crack closure, based on the David-Zimmerman model, and the squirt-flow mechanism, based on the Gurevich model. When cracks are open at low differential pressures, their properties dominate the wave velocity variations, followed by the squirt-flow mechanism. Then, a transition occurs, where cracks partially close, and the squirt-flow effect vanishes. At high pressures, cracks close and acoustoelasticity effects prevail. This behavior is observed in sedimentary rocks, whereas in granites, which have a low crack content, the acoustoelastic effect is dominant at all pressures.

Plain Language Summary It is well known that physical properties of rocks are important factors affecting the elastic wave velocities. However, how these properties affect the velocity-pressure relations are not well understood. We conducted laboratory experiments and observed that the variation of wave velocities is related to crack closure, squirt flow and acoustoelasticity effects. To study the combined effects of these mechanisms, we propose an unrelaxed double-porosity acoustoelasticity model. The theoretical results compared with the experimental data shows that, in sedimentary rocks, the crack properties dominate the pressure-dependent velocities, followed by the squirt-flow mechanism at low differential pressures. At high pressures, cracks approach full closure and the acoustoelasticity effect is the most significant. For low porosity granites, the acoustoelasticity effect dominates at all pressures.

Key Points:

- We measure elastic wave velocities in saturated rocks, to analyze the effects of crack closure, squirt flow and acoustoelasticity
- To this purpose, we develop an unrelaxed double-porosity acoustoelasticity model
- Crack closure dominates, followed by the squirt-flow mechanism at low differential pressures, while acoustoelasticity effects are important at high differential pressures. In granites, the last effect prevails

Correspondence to:
J. Ba,
jba@hhu.edu.cn

Citation:
Wei, Y., Ba, J., & Carcione, J. M. (2022). Stress effects on wave velocities of rocks: Contribution of crack closure, squirt flow and acoustoelasticity. *Journal of Geophysical Research: Solid Earth*, *127*, e2022JB025253. https://doi.org/10.1029/2022JB025253

Received 25 JUL 2022
Accepted 11 OCT 2022

Author Contributions:
Conceptualization: Jing Ba
Data curation: Yijun Wei, Jing Ba
Formal analysis: Yijun Wei, Jing Ba, José M. Carcione
Funding acquisition: Jing Ba
Investigation: Yijun Wei, Jing Ba
Methodology: Yijun Wei, Jing Ba, José M. Carcione
Project Administration: Jing Ba
Resources: Jing Ba
Software: Yijun Wei
Supervision: Jing Ba, José M. Carcione
Validation: Yijun Wei, Jing Ba, José M. Carcione
Visualization: Yijun Wei
Writing – original draft: Yijun Wei, Jing Ba

1. Introduction

Understanding the effects of stress, in particular that of differential pressure, on wave velocities of saturated rocks is of significance to detect geofluids, cracks and fractures, which is relevant in applications such as CO_2 sequestration and monitoring, disposal of nuclear wastes, aquifer investigation, reservoir exploitation and oil-gas resource development. Previous studies show that also the mineral constituents, pore structure and saturating fluids contribute to the velocity variations (Birch, 1960, 1961; Nur, 1971; Nur & Simmons, 1969; Pham et al., 2002; Simmons, 1964; Sinha & Kostek, 1996; Sinha et al., 1995).

Many experimental studies have been performed (Kuster & Toksöz, 1974; Njiekak & Schmitt, 2019; Pimienta et al., 2015, 2016; Walsh, 1965). They show that the velocities increase nonlinearly and the rate of increase decreases with differential pressure (Guo & Chen, 2022; Khaksar et al., 1999; Nur & Simmons, 1969; Wyllie et al., 1958). Smith et al. (2010) attribute this behavior to the double-porosity structure of rocks, showing that the effect is mainly due to the soft porosity (compliant pores) (Shen et al., 2020), related to cracks and grain contacts, that is, the closure of cracks implies higher velocities. Pore shape, grain contact and the crack-pore network connectivity influence the rock properties (Regnet et al., 2019). Khazanehdari and Sothcott (2003) experimentally observed that these and other factors cause significant variations of the elastic moduli, leading to stiffening or softening of the rock frame and highly affecting the wave velocities of sedimentary rocks (see also Tutuncu & Sharma, 1992). Granite, that has tighter grain contacts, presents a different behavior (Chen et al., 2009). Wang et al. (1989) measured the crack density of four granites with soft porosities ranging from 0.01% to 0.05%, and found that these porosities highly increase above 300°C. Fredrich and Wong (1986) reported a significant increase in the crack density of Westerly granite above 250°C.

Writing – review & editing: Jing Ba, José M. Carcione

King (1966) measured wave velocities of fluid-saturated sandstones and found that relaxation squirt-flow effects occur, related to the interaction between compliant pores (cracks), stiff pores and interstitial detrital material. At high frequencies, the fluid pressure between cracks and stiff pores does not equilibrate during each wave cycle, and the frame stiffens (Mavko & Nolen-Hoeksema, 1994). Mavko and Jizba (1991) considered that these effects are the main cause for this stiffening. Ba et al. (2011, 2017), Quintal et al. (2012) and L. Zhang et al. (2021, 2022) further investigated this phenomenon. Batzle et al. (2006) and Adam et al. (2006) analyzed the effects of fluids on velocities at a wide range of frequencies, and found that the fluid mobility (related to the frame permeability and fluid viscosity) has an important influence, and that the shear modulus increases with fluid saturation at ultrasonic frequencies. David et al. (2013) performed ultrasonic experiments and observed that the velocities are higher than the theoretical Gassmann velocities, except at high differential pressures. In dry sandstones, even a small amount of clay at the grain boundaries may significantly soften the grain contacts, while in saturated sandstones, wet clay stiffens and increases the grain contacts, resulting in an increase of the elastic moduli (Han et al., 1986).

On the other hand, the acoustoelasticity theory considers that the velocities depend on the stresses, and the third-order elastic constants must be introduced (Brugger, 1964; Green, 1973; Jones & Kobett, 1963; Kravchishin & Chekurin, 2009; Meegan et al., 1993). The linear theory, that is, no stress effects, has been developed by Biot (1956). Hughes and Kelly (1953) derived expressions of stress-dependent wave velocities by using Murnaghan's finite deformation theory and estimated three of those elastic constants, l, m, and n. Winkler and Liu (1996) successfully applied the theory to dry rocks. However, these constants cannot explain the velocity of water-saturated rocks (Winkler & McGowan, 2004). By generalizing Biot's theory, the poro-acoustoelasticity theory has been developed (Ba et al., 2013; Grinfeld & Norris, 1996; Guo et al., 2009).

The classical poro-acoustoelasticity theory neglects the effects of cracks and cannot well describe the pressure-dependent behavior of velocities (Winkler & Liu, 1996). Pecorari (1997) introduced the effects of cracks in the theory, and effective-medium theories were used to obtain the elastic properties (Cheng & Toksöz, 1979; Tran et al., 2008). Saenger et al. (2004) verified four of the effective-medium theories with finite-difference simulations in 3D grids, modeling cracks. They showed that the self-consistent theory predicts the P- and S-wave velocities when the crack density is less than a connectivity percolation threshold. Beyond this threshold, the differential effective-medium theory performs better. David and Zimmerman (2012) extended a previous method (Zimmerman, 1991), based on the Mori-Tanaka theory (Mori & Tanaka, 1973), and obtained the crack distribution from the pressure-dependent elastic moduli of dry rocks. Fu and Fu (2018) incorporated the effects of cracks in the theory by using an empirical equation proposed by Shapiro (2003). Ling et al. (2021) reformulated the theory, based on the effective-medium and double-porosity acoustoelasticity theories. However, these models neglect the unrelaxed (squirt-flow) effect at high frequencies (Dvorkin & Nur, 1993, Dvorkin et al., 1995; Mavko & Jizba, 1991; Murphy et al., 1986; Gurevich et al., 2009, 2010). Mavko and Jizba (1991) cannot be applied when the fluid modulus is small. Gurevich et al. (2009) solved this problem by modifying the unrelaxed moduli by using the Sayers-Kachanov discontinuity formalism.

In this work, we measure P- and S-wave velocities of dry and saturated samples. To interpret these measurements, together with the data already published, we developed an unrelaxed double-porosity acoustoelasticity model, that takes into account the effect of crack closure, squirt flow and acoustoelasticity.

2. Experiments

2.1. Rock Samples

Samples A1–A6 are collected from tight-oil reservoirs in the Upper Triassic Yanchang Formation of the Ordos Basin, west China. This formation provides the main tight sandstone oil production in that basin (Guo et al., 2012), and includes 10 members from top to bottom. The samples are taken from the Chang 7 Member, with a depth range of 1.5–3 km, which is highly productive (Yang & Zhang, 2005; Y. L. Zhang et al., 2017). The rocks are mainly fine-grained sandstones and siltstones, and the pore system is dominated by intergranular and dissolved pores (Du et al., 2019; Liao et al., 2018). The samples considered here are tight sandstones, and the main mineral composition is quartz and feldspar, with lithic fragments, and sparse carbonate minerals and clay. The grain sizes mainly range from 0.0625 to 0.25 mm.

Table 1
Properties of the Samples

Samples	Rock type	Measured by	Porosity (%)	Density (kg/m^2)
A1	Tight sandstone	This study	3.22	2,580
A2	Tight sandstone	This study	4.15	2,570
A3	Tight sandstone	This study	5.78	2,490
A4	Tight sandstone	This study	6.58	2,480
A5	Tight sandstone	This study	8.85	2,410
A6	Tight sandstone	This study	9.28	2,370
B1	Carbonate	This study	2.68	2,490
B2	Carbonate	This study	3.65	2,470
B3	Carbonate	This study	4.11	2,510
B4	Carbonate	This study	4.44	2,714
B5	Carbonate	This study	10.37	2,552
B6	Carbonate	This study	17.35	2,328
C1	Granite	Chen et al. (2009)	0.2	2,700
C2	Granite	Coyner (1984)	0.8	2,641
C3	Sandstone	Coyner (1984)	9.5	2,391
C4	Sandstone	Coyner (1984)	17.8	2,197

Samples B1–B3 are collected from a carbonate reservoir in the lower Ordovician Yingshan Formation of the Shunnan area of Tarim Basin, west China. The depth exceeds 7 km, and the temperature and differential pressure are greater than 150°C and 60 MPa, respectively. The hydrothermal minerals and dissolution of the lower Yingshan Formation are relatively well-developed, and this activity leads to a strong dolomitization (Liu et al., 2021). The reservoir is mostly composed of dolomite and limy dolomite, with fine-to-medium grain size (Zhao et al., 2018), while the porosity ranges from 0.2% to 5%. The pore space mainly consists of dolomite micropores, and intercrystalline and solution pores.

Samples B4–B6 are collected from the carbonate reservoirs of the Middle Triassic Leikoupo Formation of Sichuan Basin, China. The depth of the target layer is greater than 5.5 km and the in situ reservoir temperature is around 120°C. The lithology is mainly dolomicrite, fine crystalline dolomite and argillaceous algal-dolomite (Li et al., 2020). Intergranular pores and microcracks are developed, and some pores are filled with dolomite cements. Dissolution pores and microcracks constitute the main reservoir space, with a porosity higher than 2%.

The data of samples C1–C4 are reported by Chen et al. (2009) and Coyner (1984). Sample C1 is a fine-grained granite with the grain sizes of about 1 mm. Sample C2 is a medium-grained granite, and the main mineral compositions are potassium feldspar, plagioclase and quartz, with feldspar grains of sizes up to 5 mm. Sample C3 is a dark brown colored, very fine-grained sandstone, with sub-rounded grains. Sample C4 is a light buff-gray colored, fine-grained sandstone with a quartz content up to 76%.

The physical properties of the 16 samples are given in Table 1. The porosity of the samples is measured by the gas-expansion method by using the automated permeameter of core measurement system, and the dry-rock density is obtained as the ratio of the rock mass to the total volume. The mineralogy of samples is given in Table 2.

2.2. Experimental Setup

The experimental setup is based on that of Guo et al. (2009), which consists of a pulse generator (Panametrics 5077PR), a digital oscilloscope (Tektronix TDS 420 A) and a computer-aided control device. The computer

Table 2
Mineral Contents of Samples

Samples	Quartz (%)	Feldspar (%)	Calcite (%)	Dolomite (%)	Siderite (%)	Clay (%)	Silicalite (%)
A1	51.71	27.49	0.56	11	3.21	6.03	–
A2	52.87	24.92	2.91	10.97	1.17	7.16	–
A3	51.42	27.26	6.78	5.69	2.62	6.23	–
A4	56.81	21.59	1.96	10.92	2.12	6.6	–
A5	53.88	31.61	1.95	6.14	1.07	5.35	–
A6	53.73	23.92	4.77	8.67	1.75	7.16	–
B1	20	–	–	60	–	–	20
B2	15	–	–	65	–	–	20
B3	10	–	–	75	–	–	15
B4	0.2	0.4	0.7	98.09	–	0.61	–
B5	0.23	0.29	0.97	97.85	–	0.66	–
B6	0.16	0.29	0.83	97.72	–	1.00	–

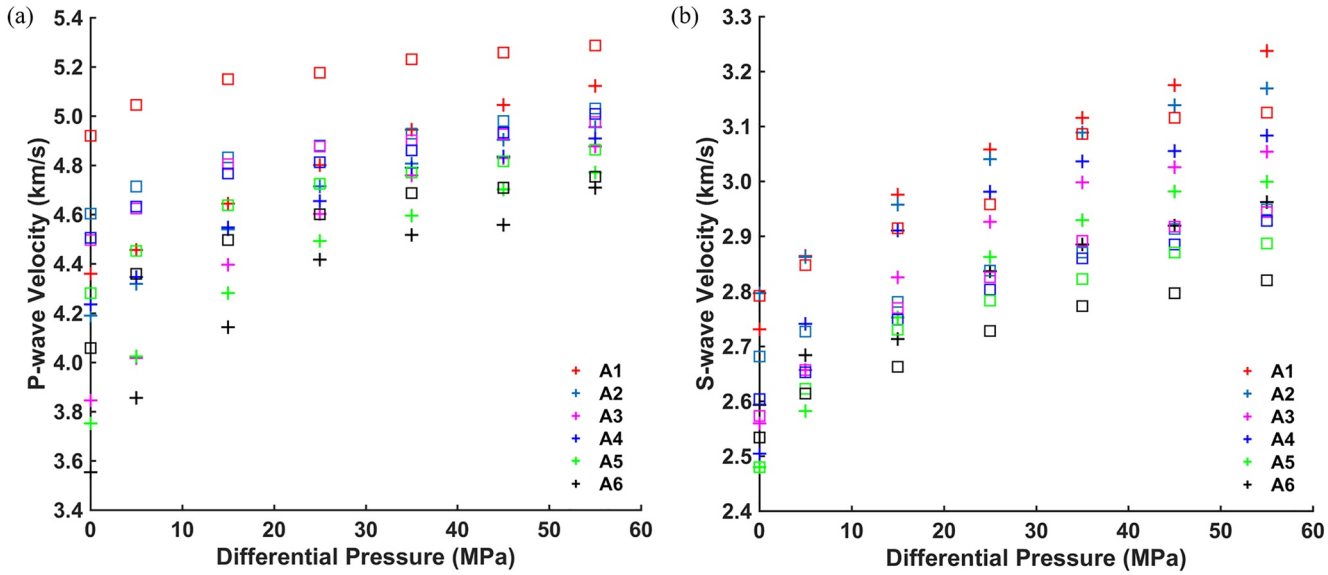

Figure 1. P-wave (a) and S-wave velocities (b) of samples A1–A6 as a function of differential pressure. The symbol "+" represents dry-rock data, and the squares indicate brine-saturated data.

control system includes a separate control unit of temperature, confining and pore pressure and fluid saturation. The ultrasonic wave velocities can be measured under confining pressures and temperature up to 90 MPa and 150°C. We obtained the velocities for dry and water-saturated conditions at variable differential pressure, based on the ultrasonic pulse transmission method (Birch, 1960).

Samples A1–A6 are first dried in an oven at 80°C for 36 hr, and then sealed with rubber jackets and placed into the pressure vessel after natural cooling. The confining pressures are 5, 10, 20, 30, 40, 50, and 60 MPa, and the pore pressure is 5 MPa. The samples are saturated with brine by the vacuum and pressure-saturation method (Kristinsdóttir et al., 2010) and sealed with rubber jackets. The same temperature, confining pressures and pore pressure as above are set. The bulk modulus of brine is 2.244 GPa, estimated with the Batzle-Wang equation

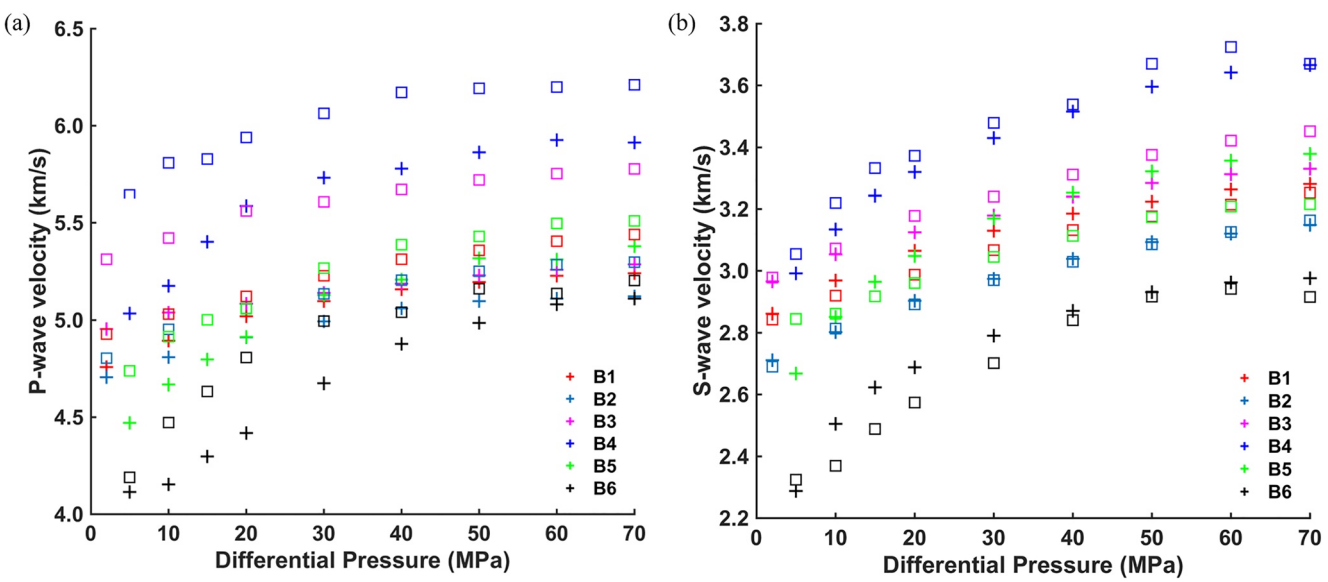

Figure 2. P-wave (a) and S-wave velocities (b) of samples B1–B6 as a function of differential pressure. The symbol "+" represents dry-rock data, and the squares indicate brine-saturated data.

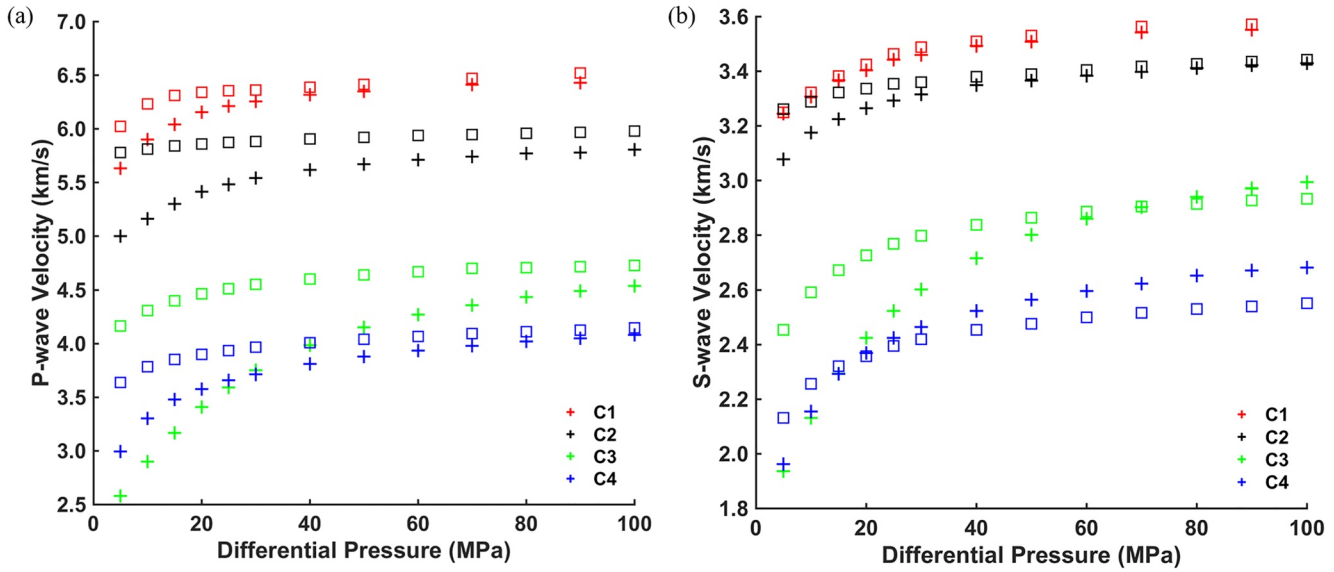

Figure 3. P-wave (a) and S-wave velocities (b) of samples C1–C4 as a function of differential pressure. The symbol "+" represents dry-rock data, and the squares indicate water (distilled water)-saturated data.

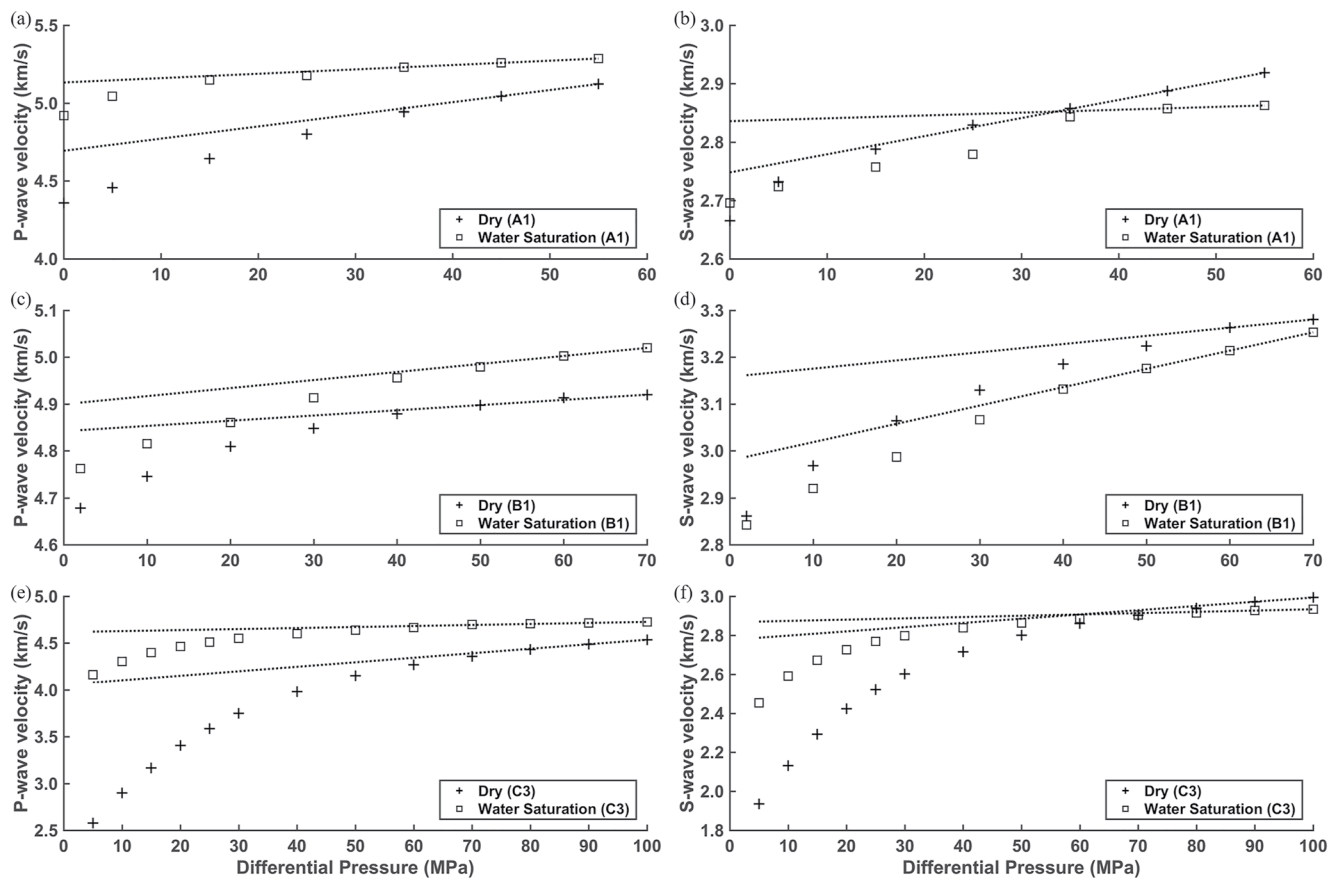

Figure 4. P- and S-wave velocities of the three typical samples as a function of differential pressure. The symbol "+" represents dry-rock data, the squares water-saturated data and the dotted lines a linear fit at high pressures. (a) P-wave velocity of sample A1; (b) S-wave velocity of sample A1; (c) P-wave velocity of sample B1; (d) S-wave velocity of sample B1; (e) P-wave velocity of sample C3; (f) S-wave velocity of sample C3.

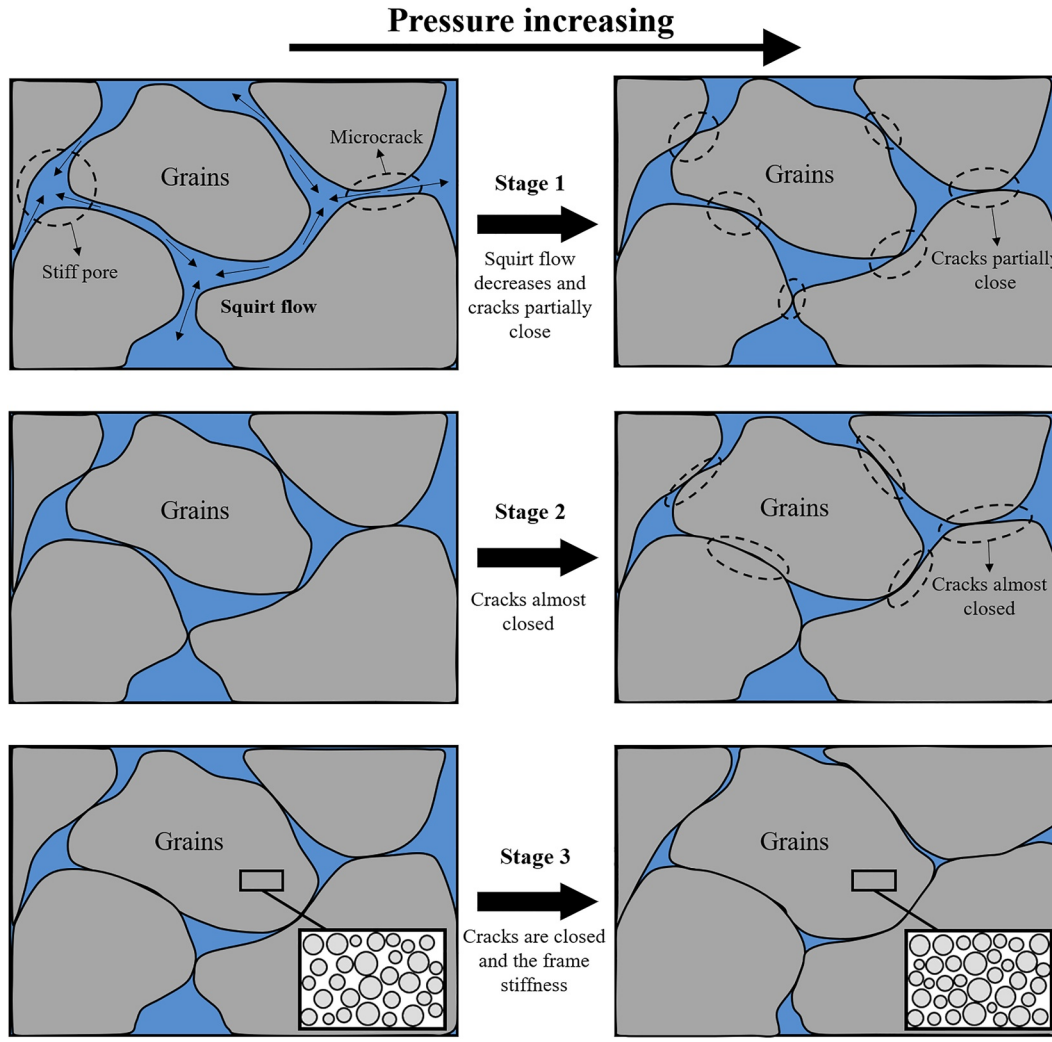

Figure 5. Diagram of how the microstructure of a saturated rock is affected by the differential pressure.

(Batzle & Wang, 1992) (see Appendix B). The P- and S-wave velocities are computed from the initial arrivals of the waveforms.

The experimental process of samples B1–B6 is the same. In this case, the confining pressures applied to samples B1–B3 are 12, 20, 30, 40, 50, 60, 70, and 80 MPa, and those of samples B4–B6 are 15, 20, 30, 40, 50, 60, 70, and 80 MPa. The pore pressure and the temperature of all the samples are 10 MPa and 130°C (close to the in situ temperature), respectively. The bulk modulus of brine is 2.19 GPa.

On the other hand, a detailed description of the experimental setup for samples C1–C4 can be found in Chen et al. (2009) and Coyner (1984). The dry-rock and fluid (distilled water)-saturated P- and S-wave velocities were measured at room temperature, and the differential pressures were set at 5, 10, 15, 20, 30, 40, 60, and 80 MPa for sample C1 and 5, 10, 15, 20, 25, 30, 40, 50, 60, 70, 80, 90, and 100 MPa for samples C2–C4. The pore fluid is distilled water and the pore pressure is 10 MPa.

2.3. Velocity-Pressure Relations

Figures 1–3 show the P- and S-wave velocities as a function of differential pressure for dry and water-saturated conditions. The P-wave velocities of all the 16 samples and the S-wave velocities of samples B3, B4, C1, C2,

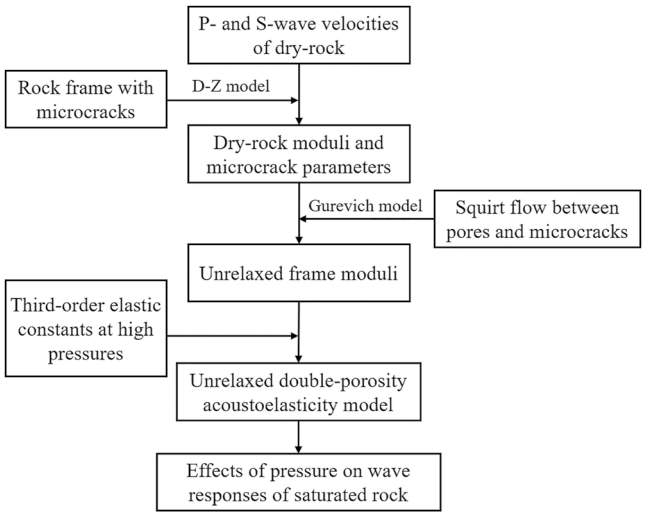

Figure 6. Flowchart for the proposed model. D-Z denotes the David-Zimmerman model.

and C3 increase with water saturation, while for samples A1-6, B1, B2, B5, B6, and C4, the wet-rock S-wave velocities are less than the dry-rock ones. The Gassmann equation (Gassmann, 1951) has been widely applied for fluid substitution, where the shear modulus of the rock remains the same after saturation. The average density of a saturated rock is higher than that of a dry rock, thus the S-wave velocity decreases with saturation. However, Mavko and Jizba (1991) interpreted that the S-wave velocity increase with water saturation is due to unrelaxation effects. The velocity shows different behaviors at low and high differential pressures, as shown in Figure 4, where it is nearly linear at high pressures and nonlinear at low values. Studies attribute these behaviors to the closure of cracks (Deng et al., 2015; Shapiro, 2003).

3. Modeling Pressure-Dependent Wave Velocities

3.1. Poro-Acoustoelasticity Theory

The conventional theory describes the wet-rock P-wave and shear moduli under loading stresses in the rock with non-compliant pores (Ba et al., 2013),

$$\begin{cases} \rho V_{\mathrm{P}}^2 = \left(K_m + M\gamma^2 + \frac{4}{3}G_m\right) + \Psi_1\alpha + \Psi_2\beta \\ \rho V_{\mathrm{S}}^2 = G_m + \Psi_3\alpha + \Psi_4\beta \end{cases}, \tag{1}$$

where V_{P} and V_{S} are the corresponding velocities, $M = \frac{K_g}{1-\phi-K_m/K_g+\phi K_g/K_f}$, $\gamma = 1 - K_m/K_g$, K_g, K_m and K_f are the bulk moduli of the grains (mineral), matrix (frame) and fluid, respectively, ϕ is the total porosity, G_m is the dry-rock shear modulus, $\rho = \rho_{11} + 2\rho_{12} + \rho_{22} = (1-\phi)\rho_g + \phi\rho_f$ is the bulk density (Biot, 1962), ρ_g and ρ_f are the grain and fluid densities, respectively, and α and β are the solid and fluid stress components, respectively, given by Ba et al. (2013), Fu and Fu (2018), and Ling et al. (2020)

$$\begin{cases} \alpha = \dfrac{P_{\mathrm{c}} - \phi P_{\mathrm{f}}}{3(1-\phi)K_{\mathrm{g}}} \\ \beta = \dfrac{\theta - 3(1-\phi)\alpha}{3\phi} \end{cases}, \tag{2}$$

where P_{c} and P_{f} are the confining and pore pressures, respectively, and $\theta = \frac{P_{\mathrm{c}} - \gamma P_{\mathrm{f}}}{K_m}$ is the elastic bulk strain. Ψ_i ($i = 1, 2, 3, 4$) in Equation 1 are third-order elastic constants, given by Ling et al. (2020)

$$\begin{cases} \Psi_1 = 7K_m + \frac{16}{3}G_m + 7M\gamma(\gamma-\phi) + 9M_5 + 2M_8 + 2M_9 + 6M_{10} + 3M_{11} \\ \Psi_2 = 7M\gamma\phi + 9M_7 + 3M_{10} + 6M_{11} \\ \Psi_3 = 3K_m + 4G_m + 3M(\gamma-\phi)^2 - \frac{1}{4}M_6 - \frac{3}{4}M_8 \\ \Psi_4 = 3M\phi(\gamma-\phi) - \frac{3}{4}M_9 \end{cases}, \tag{3}$$

where M_5, M_6, and M_8 are related to the solid, M_7 is related to the pore fluid, and M_9, M_{10} and M_{11} to the fluid-solid coupling.

3.2. Effective-Medium Model With Cracks

The poro-acoustoelasticity theory does not consider cracks. The effective-medium theory is adopted to add cracks into the rock frame for obtaining the dry-rock moduli. The stiff bulk and shear moduli (cracks closed) are given by Mori & Tanaka (1973).

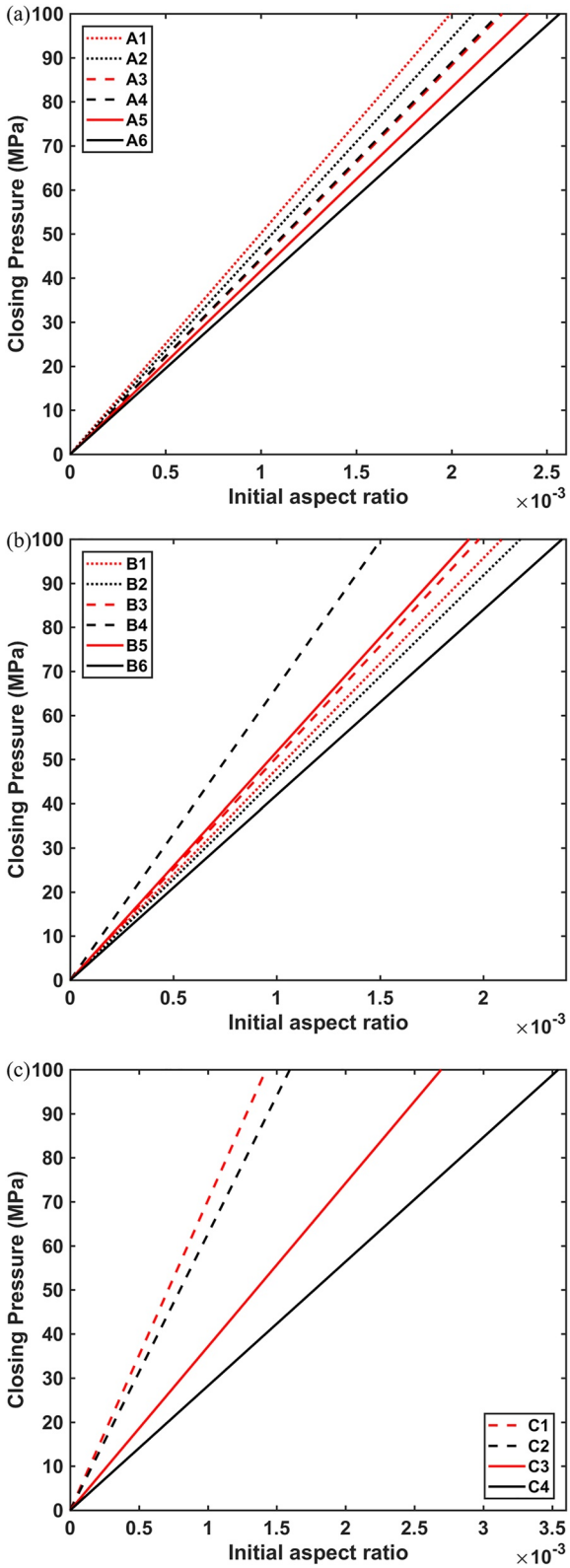

Figure 7. Pressure required to close the crack as a function of the initial aspect ratio for samples A1–A6 (a), B1–B6 (b) and C1–C4 (c).

$$K_{\text{stiff}} = K_g \Big/ \left(1 + \frac{\phi_{\text{stiff}}}{1-\phi_{\text{stiff}}} P\right), \tag{4}$$

$$G_{\text{stiff}} = G_g \Big/ \left(1 + \frac{\phi_{\text{stiff}}}{1-\phi_{\text{stiff}}} Q\right), \tag{5}$$

where G_g is the grain shear modulus. The grain moduli K_g and G_g are given by the Voigt-Reuss-Hill average (Hill, 1952; Reuss, 1929; Voigt, 1910). ϕ_{stiff} is the stiff porosity. P and Q are shape factors (see Appendix A). By assuming that cracks close at high differential pressures, K_{stiff} and G_{stiff} can be estimated from the P- and S-wave velocities.

Then, the effective dry-rock bulk and shear moduli are respectively (Mori & Tanaka, 1973),

$$K_m = K_{\text{stiff}} \Big/ \left(1 + \frac{16(1-(\upsilon_{\text{stiff}})^2)\Gamma}{9(1-2\upsilon_{\text{stiff}})}\right), \tag{6}$$

$$G_m = G_{\text{stiff}} \Big/ \left(1 + \frac{32(1-\upsilon_{\text{stiff}})(5-\upsilon_{\text{stiff}})\Gamma}{45(2-\upsilon_{\text{stiff}})}\right), \tag{7}$$

where $\upsilon_{\text{stiff}} = (3K_{\text{stiff}} - 2G_{\text{stiff}}) / (6K_{\text{stiff}} + 2G_{\text{stiff}})$ is the stiff-pore Poisson ratio, and Γ is the cumulative crack density (total number of cracks embedded in a unit volume). The elastic moduli can be obtained from the velocities at different differential pressures. Then, the pressure-dependent crack density $\Gamma_P(\alpha)$ can be computed by a least-square regression based on the elastic parameters obtained from Equations 6 and 7 and the dry-rock velocities.

David and Zimmerman (2012) provided an empirical relation between crack density and differential pressure P as

$$\Gamma_P = \Gamma_0 \mathrm{e}^{-P/\hat{P}}, \tag{8}$$

where Γ_0 is the initial crack density, and $\hat{P}$ is a compaction coefficient, which can be obtained by fitting data with Equations 6 and 7.

The relation between crack density and crack porosity is (David & Zimmerman, 2012; Vernik & Kachanov, 2010)

$$\phi_c(P) = \frac{4\pi\alpha_P}{3}\Gamma_P. \tag{9}$$

Moreover, the relation between the pore aspect ratio and the differential pressure is (David & Zimmerman, 2012; L. Zhang et al., 2019)

$$\alpha_P = \frac{4\left[1-(\nu_m)^2\right]P}{\pi E_m}, \tag{10}$$

where $\upsilon_m = (3K_m - 2G_m) / (6K_m + 2G_m)$ and $E_m = 3K_m[1 - 2\upsilon_m]$ are the effective Poisson ratio and Young modulus.

3.3. Squirt-Flow Theory

At the high frequency range, there is a pore fluid pressure gradient between the stiff and compliant pores caused by the acoustic waves and the rock is in unrelaxed state. Gurevich et al. (2010) obtained the unrelaxed bulk and shear compliances,

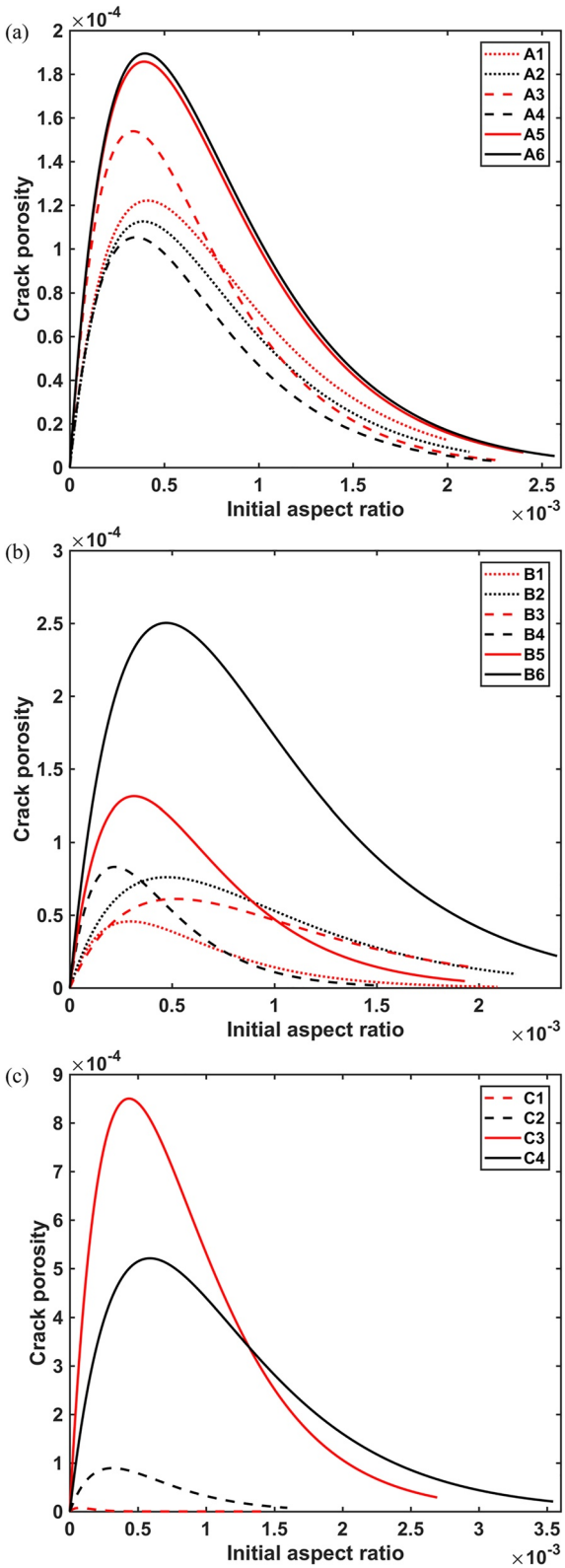

Figure 8. Porosity distribution as a function of the initial aspect ratio for samples A1–A6 (a), B1–B6 (b) and C1–C4 (c).

$$\frac{1}{K_{uf}(P)} = \frac{1}{K_{\text{stiff}}} + \frac{1}{\left(K_m(P)^{-1} - K_{\text{stiff}}^{-1}\right)^{-1} + \left(\left(K_f^{-1} - K_g^{-1}\right)\phi_c(P)\right)^{-1}}, \quad (11a)$$

$$\frac{1}{G_{uf}(P)} = \frac{1}{G_m(P)} - \frac{4}{15}\left(K_m(P)^{-1} - K_{uf}(P)^{-1}\right), \quad (11b)$$

respectively (the moduli are the reciprocal). For dry rock, K_f is zero and the term $\left(\left(K_f^{-1} - K_g^{-1}\right)\phi_c(P)\right)^{-1}$ can be neglected, so that K_{uf} and G_{uf} are equal to the dry-rock moduli K_m and G_m, respectively. When the differential pressure is high enough and cracks close, ϕ_c approaches zero, the term $\left(\left(K_f^{-1} - K_g^{-1}\right)\phi_c(P)\right)^{-1}$ is infinity, and K_{uf} and G_{uf} are equal to K_{stiff} and G_{stiff}, respectively, as expected.

3.4. Unrelaxed Double-Porosity Acoustoelasticity Model

Figure 5 illustrates how the microstructure of a saturated rock is affected by the differential pressure. There are stiff pores and compliance cracks between grain boundaries (Shen et al., 2020). Tight grain-to-grain contact increase the bulk and shear moduli and thus the wave velocities. The cracks gradually close with pressure increase and stiffen the frame (Zaitseva et al., 2017). In addition, the squirt flow between pores and cracks also stiffens the frame at high (ultrasonic) frequencies (Sun & Gurevich, 2020). We consider these factors and the effect of the loading stress. Figure shows three stages. In stage 1, the fluid pressure gradient stiffens the frame at high frequencies. At this stage, cracks start to close and squirt flow decreases with the pressure increase. In stage 2, when cracks approach a partial-closure state, the squirt-flow mechanism tends to disappear, and crack effects dominate. In stage 3, the cracks have almostly completed closed and the acoustoelasticity effect prevails.

The workflow to model the behaviors of the data is shown in Figure 6. First, the crack properties and dry-rock moduli are obtained based on the dry-rock wave velocities (Ling et al., 2020). Then, the unrelaxed frame moduli are obtained by using the Gurevich model (Equation 11). The elasticity constants Ψ_i can be estimated from two sets of wave velocities at high differential pressures. Then, moduli and constants Ψ_i are substituted into Equation 1 to obtain the pressure-dependent wet rock P- and S-wave moduli as

$$\begin{cases} \rho V_{\text{P}}^2 = \left(K_{uf} + M_{uf}\gamma_{uf}^2 + \frac{4}{3}G_{uf}\right) + \Psi_1\alpha + \Psi_2\beta \\ \rho V_{\text{S}}^2 = G_{uf} + \Psi_3\alpha + \Psi_4\beta \end{cases}, \quad (12)$$

where $M_{uf} = \frac{K_g}{1-\phi-K_{uf}/K_g+\phi K_g/K_f}$, and $\gamma_{uf} = 1 - K_{uf}/K_g$.

For a dry rock, the unrelaxed and dry-rock moduli are the same and Equation 12 corresponds to the double-porosity acoustoelasticity model (Ling et al., 2020). When the differential pressure $P \to \infty$, $\phi_c(P) \to 0$, the unrelaxed moduli are equal to the moduli with only stiff pores, and Equation 12 gives the classical poro-acoustoelasticity model (Equation 1).

The almost linear variation of velocity at the high differential-pressure range is consistent with the poro-acoustoelasticity model, which assumes that the

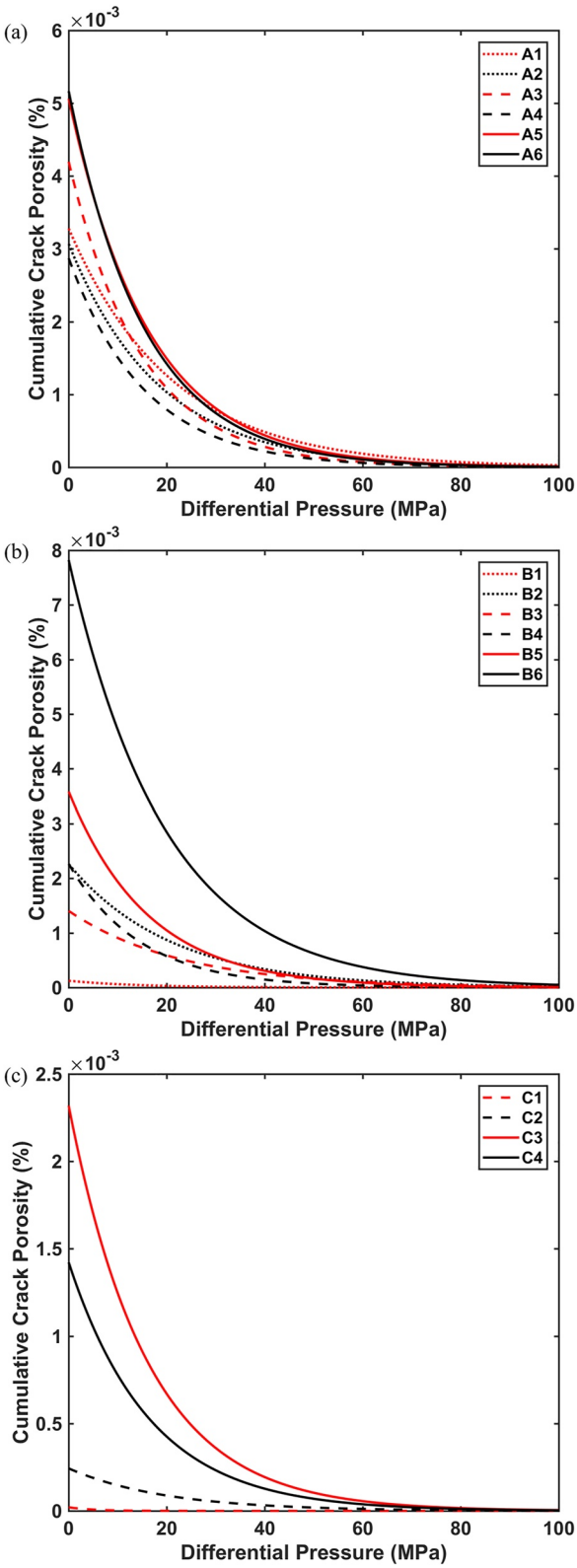

Figure 9. Cumulative crack porosity as a function of the differential pressure for samples A1–A6 (a), B1–B6 (b) and C1–C4 (c).

rock microstructure is constant (Fu & Fu, 2018). The elastic constants Ψ_i can be estimated from the velocities at that range, as well as α and β,

$$\begin{cases} \alpha^{hp} = \dfrac{P_c^{hp} - \phi P_f}{3(1-\phi)K_g} \\ \beta^{hp} = \dfrac{\theta^{hp} - 3(1-\phi)\alpha^{hp}}{3\phi} \end{cases}, \tag{13}$$

where $\theta^{hp} = \frac{P_c^{hp} - (1 - K_{stiff}/K_g)P_f}{K_{stiff}}$ is the elastic bulk strain. The experimental data $(V_{P,sat}^{hp1}; V_{S,sat}^{hp1})$ and $(V_{P,sat}^{hp2}; V_{S,sat}^{hp2})$ for saturated rocks corresponding to the two values of high pressures P_c^{hp1} and P_c^{hp2} can be replaced in Equation 12, and Ψ_i are obtained.

4. Results

4.1. Crack Properties

The pressure dependence of the elastic properties depends on the crack aspect ratio. Walsh (1965) proposed a relation between the initial aspect ratio α_i and the pressure required to close the crack, that is,

$$P_{close} = \frac{\pi E_{stiff} \alpha_i}{4\left(1 - v_{stiff}^2\right)}. \tag{14}$$

where E_{stiff} is the Young modulus when cracks are closed. Relation 14 is graphically shown in Figure 7, where P_{close} increases linearly with the aspect ratio. The crack properties are shown in Figures 8–10 (see Section 3.2). Figure 8 shows the porosity distribution as a function of the aspect ratio. The samples with a higher porosity exhibit a higher crack content and a wider aspect-ratio range. Figures 9 and 10 show that the cumulative crack porosity and density decrease nonlinearly with differential pressure. The decrease rate is pronounced at low differential pressure range. The sandstone samples show higher crack densities, followed by the tight-sandstone and carbonate ones, while the granites have the lowest crack content, approaching zero at about 40 MPa.

4.2. Bulk and Shear Moduli

Previous works showed that compliant pores with an aspect ratio less than 0.01 have a significant effect on the second-order elastic moduli (Guéguen & Sarout, 2009, 2011; Mavko et al., 2009; Sarout, 2012). By using Equations 6 and 7, the dry-rock moduli with the effects of cracks are obtained. Figure 11 shows that the bulk and shear moduli increase with differential pressure. To incorporate the effect of squirt flow, the dry-rock crack properties and moduli are replaced in Equation 11 to obtain the unrelaxed frame moduli, represented in Figure 12. A comparison between Figures 11 and 12 shows that the unrelaxed bulk/shear moduli are higher than those of the dry rock, indicating a stiffening due to the pore fluid. The increase rate of unrelaxed moduli is lower than that of the dry-rock moduli, indicating that the effect of stress on the cracks in a saturated rock is weaker than that in a dry rock, which may be related to the clay swelling caused by water saturation which increase the grain contacts (Han et al., 1986).

The second-order elastic constants can be obtained from the experimental data. The elastic strains α and β are computed by using the two sets of

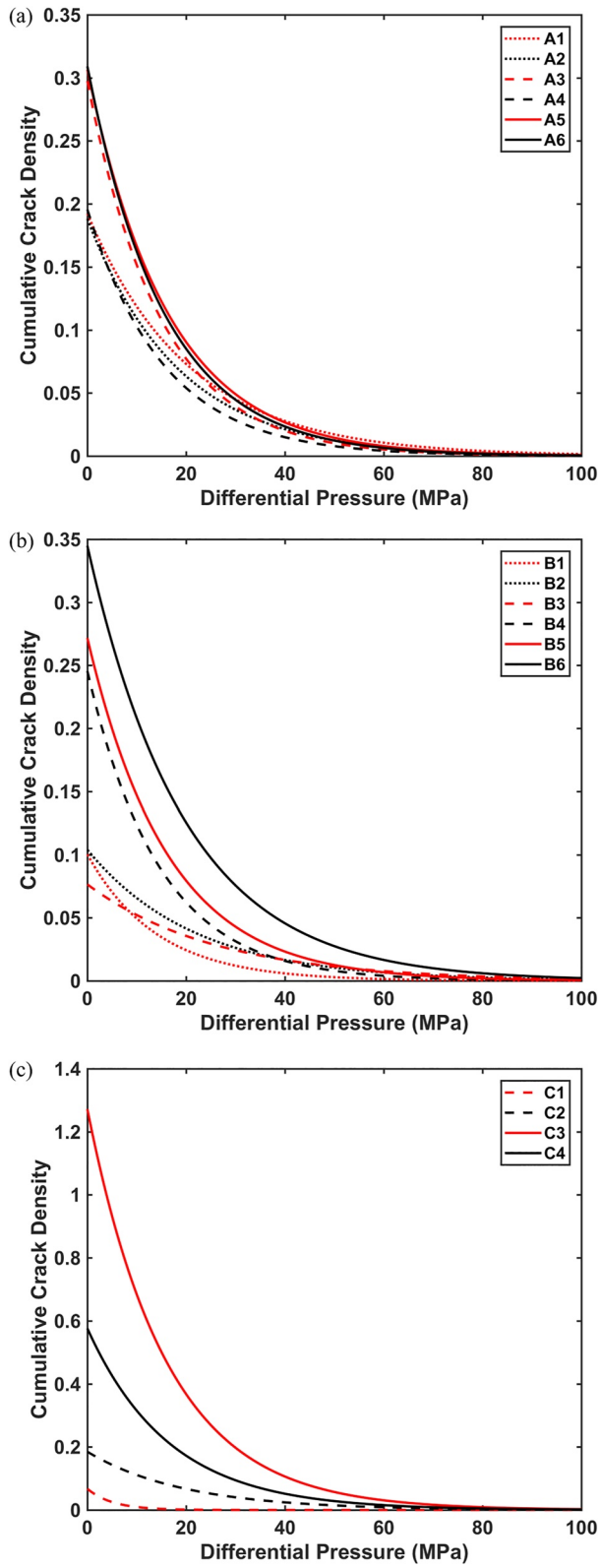

Figure 10. Cumulative crack density as a function of the differential pressure for samples A1–A6 (a), B1–B6 (b) and C1–C4 (c).

wet-rock velocities at high differential pressures, and are replaced in Equation 12 to obtain the elastic constants Ψ_i, which are shown in Table 3.

4.3. Pressure-Dependent Velocities

The results of the proposed model and that of the double-porosity acoustoelasticity model are the same for a dry rock, since the fluid modulus is zero. Figure 13 shows the results, where the solid and dashed lines correspond to the present model and poro-acoustoelasticity model, respectively, which are basically consistent at high differential pressures and are in good agreement with the experimental data. At low differential pressures, the proposed model performs better.

In Figures 14–16, the solid, dotted and dashed lines refer to the present model, and double-porosity acoustoelasticity model and poro-acoustoelasticity model, respectively. The results of the three models agree well with the data at the high pressures, and the P-wave velocity of the present model agrees better at low pressures. For samples B2, B5, and B6, the double-porosity acoustoelasticity model and the present model fairly predict the S-wave velocity, which means that, for these samples, the fluid unrelaxation effect on the shear modulus is weak. For the granite sample C1, both the first and third models are consistent with the P-wave velocities, which may be associated with the weak squirt-flow effect due to the low crack content and tight grain contacts.

4.4. Effects of Crack Closure, Squirt Flow and Acoustoelasiticty

Figures 14–16 show that when the differential pressure exceeds a certain threshold, the predictions of the three models are consistent. We consider two threshold pressures: that of crack closure, P_1, and that when the squirt-flow effect vanishes, P_2. When the pressure exceeds P_1, cracks close and the double- and single-porosity results coincide. Beyond P_2, the squirt-flow effect can be neglected, and the predictions of the proposed model coincide with those of the double-porosity one. In this work, the relative difference less than 1% between two models is defined as an almost coincidence, and the threshold pressures for each sample are shown in Figure 17, where the solid circles represent P_1 and the empty ones P_2. P_2 is smaller than P_1, which indicates that the cracks are not fully (partially) closed in the absence of squirt flow. It can be seen that the threshold pressure is higher for the more porous samples. The threshold pressures for granite C1 (with almost no soft pores) are both less than 20 MPa.

To quantify the effects of the three mechanisms on the pressure-dependent velocities, we estimate the velocity variation with respect to pressure change for each model, and then compute the ratio of the variation of each model to the total variation of measurement as

$$R1 = \left[\left(V_{\mathrm{P},2}^{(P_{\max})} - V_{\mathrm{P},2}^{(P_i)}\right) - \left(V_{\mathrm{P},3}^{(P_{\max})} - V_{\mathrm{P},3}^{(P_i)}\right)\right] / \left(V_{\mathrm{P}}^{(P_{\max})} - V_{\mathrm{P}}^{(P_i)}\right), \quad (15)$$

$$R2 = \left[\left(V_{\mathrm{P},1}^{(P_{\max})} - V_{\mathrm{P},1}^{(P_i)}\right) - \left(V_{\mathrm{P},2}^{(P_{\max})} - V_{\mathrm{P},2}^{(P_i)}\right)\right] / \left(V_{\mathrm{P}}^{(P_{\max})} - V_{\mathrm{P}}^{(P_i)}\right), \quad (16)$$

$$R3 = \left(V_{\mathrm{P},3}^{(P_{\max})} - V_{\mathrm{P},3}^{(P_i)}\right) / \left(V_{\mathrm{P}}^{(P_{\max})} - V_{\mathrm{P}}^{(P_i)}\right), \quad (17)$$

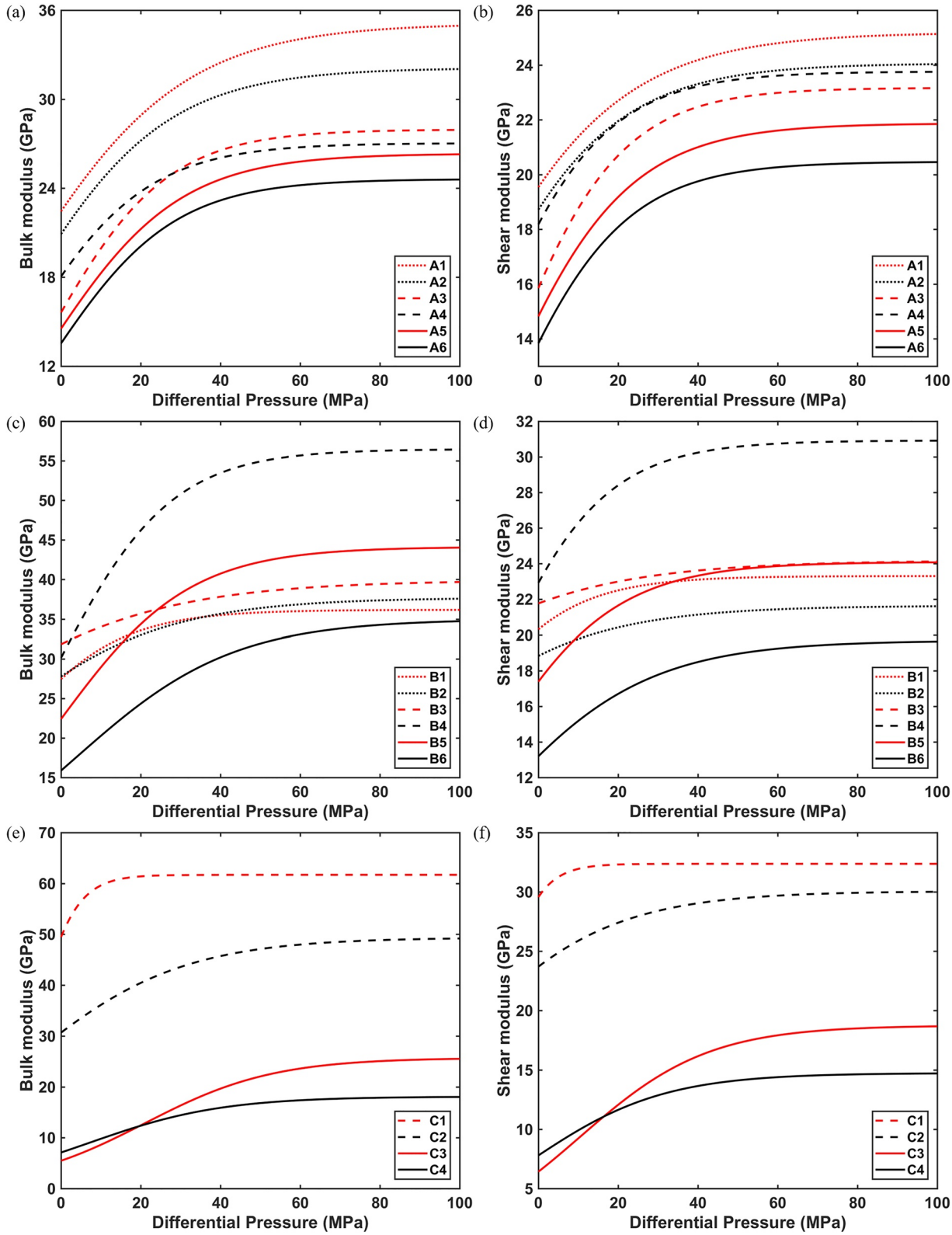

Figure 11. Dry-rock bulk and shear moduli as a function of the differential pressure for the various samples. (a) Bulk moduli of A1–A6; (b) Shear moduli of A1–A6; (c) Bulk moduli of B1–B6; (d) Shear moduli of B1–B6; (e) Bulk moduli of C1–C4; (f) Shear moduli of C1–C4.

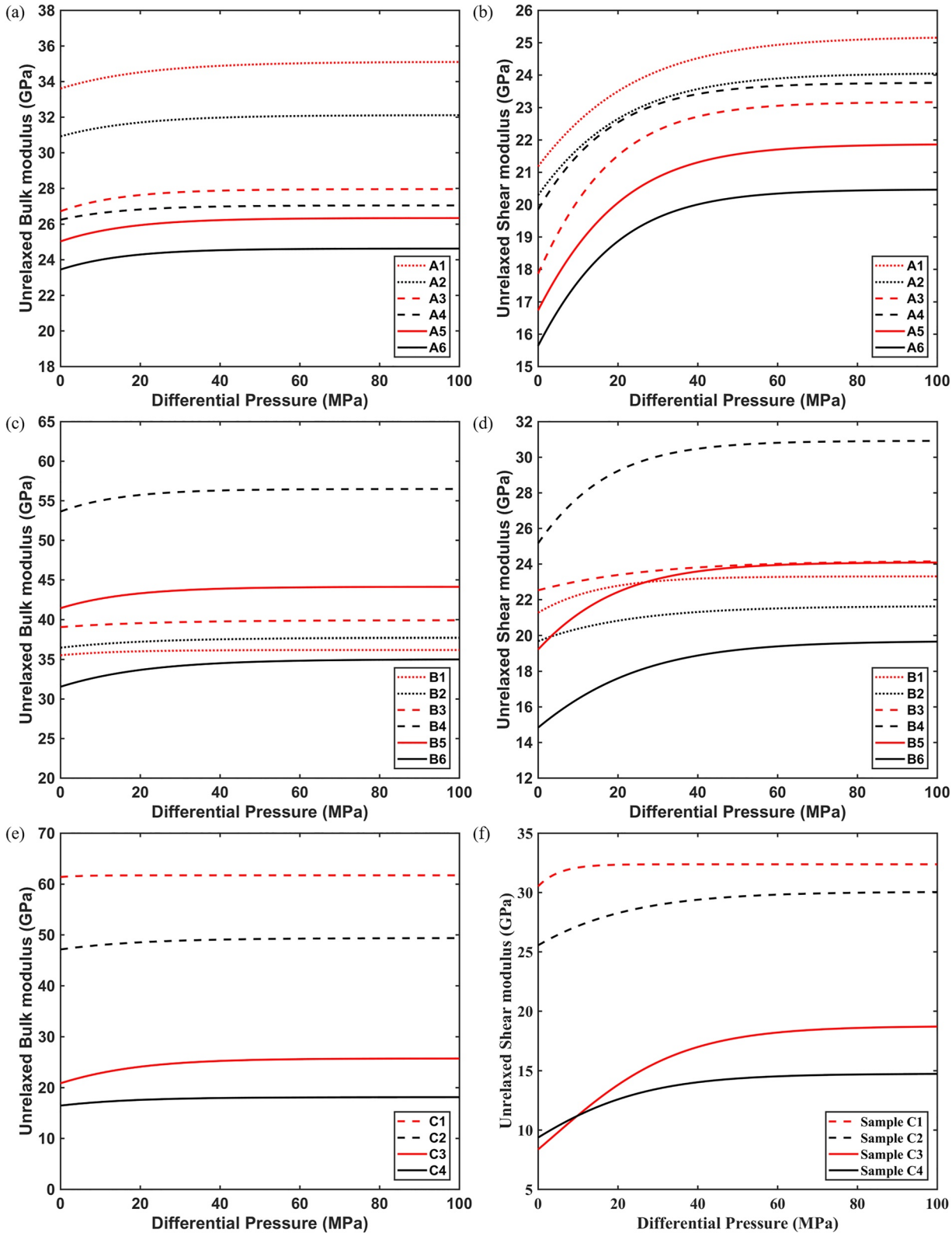

Figure 12. Unrelaxed bulk and shear moduli as a function of the differential pressure for the various samples. (a) Unrelaxed bulk moduli of A1–A6; (b) Unrelaxed shear moduli of A1–A6; (c) Unrelaxed bulk moduli of B1–B6; (d) Unrelaxed shear moduli of B1–B6; (e) Unrelaxed bulk moduli of C1–C4; (f) Unrelaxed shear moduli of C1–C4.

Table 3
Elastic Constants Ψ_i (i = 1, 2, 3, 4) for the 16 Samples

Samples	Ψ_1 (GPa)	Ψ_2 (GPa)	Ψ_3 (GPa)	Ψ_4 (GPa)
A1	−36,473.6	6,600.04	−9,926.13	1,706.395
A2	−131,311	19,587.94	−68597	9,969.449
A3	−107,201	13,674.16	−50984.5	6,219.862
A4	−152,758	20,492.36	−85588.8	10,869.51
A5	−94,794.6	17,844.22	−37630.3	6,684.36
A6	−96,037.4	14,703.57	−43301.3	6,400.717
B1	−245,202	8,012.644	−4,245.48	143.996
B2	−225,349	8,927.924	−18561.9	1,207.779
B3	−41,034.8	2,906.157	−16548.6	1,189.863
B4	33,347.96	−4,673.63	76.41031	166.2477
B5	−35,413.3	7,769.25	60,930.47	−10663.5
B6	−261,223	52,528.53	40,911.94	−7,331.22
C1	−286,370	131,787.4	16,889.83	−5,810.97
C2	−17,472.1	1,412.411	2,695.598	−46.517
C3	714.3241	424.1006	24,201.63	−5,095.43
C4	−48,812.4	12,087.94	−9,399.13	2,452.421

corresponding to the contributions of crack closure, squirt flow and acoustoelasticity, respectively, where $V_{P,1}$, $V_{P,2}$, and $V_{P,3}$ are the P-wave velocities predicted by the present model, double-porosity acoustoelasticity model and poro-acoustoelasticity model, respectively, and V_P is the experimental velocity. The superscripts P_{max} and P_i refer the maxim differential pressure in the analysis scope and the differential pressure considered, respectively.

Figures 18–20 show the three contributions as a function of the differential pressure. In the initial stage of loading stress, the samples with higher porosity generally present a higher contribution value due to the crack closure and squirt-flow effect and a lower contribution of acoustoelasticity, with the first one higher than the second one. With the increase of pressure, contributions of crack closure and squirt flow decrease and approaches zero, while that of acoustoelasticity increases. These results, corresponding to the three deformation stages of the rock microstructure, can be described by the threshold pressures. In stage 1 ($P < P_2$), the coupling effects of three mechanisms affect the velocities, and crack effects are dominant, followed by that of squirt flow and acoustocelasticity. In stage 2 ($P_2 < P < P_1$), the squirt-flow effect vanishes, and cracks and acoustoelasticity dominate. In stage 3 ($P > P_1$), the latter prevails.

Figure 21 displays a histogram of the mean contribution variation for the four different lithologies. The variations for crack closure and squirt flow in sandstone, tight sandstone and carbonate rocks are greater than those in granite. This indicates that the pressure-dependent velocity of sedimentary rocks is strongly influenced by the presence of cracks, and the effect is especially pronounced in sandstone with a higher porosity range. For granite with low porosity, low crack content and tight grain contacts, the acoustoelasticity effect in the solid phase dominates.

5. Conclusions

We have developed an unrelaxed double-porosity acoustoelasticity model to predict the P- and S-wave velocities as a function of the differential pressure, including the effects of (micro) crack closure, squirt flow and acoustoelasticity. We have performed ultrasonic experiments under dry and water-saturated conditions, and compared theory and experiment based on the test data, together with data already published. The velocities increase nonlinearly with differential pressure at the initial loading stage, and the rate approaching a constant when the cracks close. The pore fluid stiffens the grain contacts and rock frame (unrelaxation due to squirt flow), resulting in a higher P-wave velocity than that of the dry rock. This effect also leads to the increase of shear modulus and S-wave velocity.

The effects of crack closure, squirt flow and acoustoelasticity on the velocities of the sedimentary rocks can be divided into three loading regimes. Initially (low differential pressure) the cracks properties dominate, followed by the squirt-flow mechanism. Then, the squirt-flow effect vanishes and crack effects are dominant. Finally, at high differential pressures, the acoustoelasticity effect prevails. For low porosity granite, the acoustoelasticity effect is dominant at all three stages.

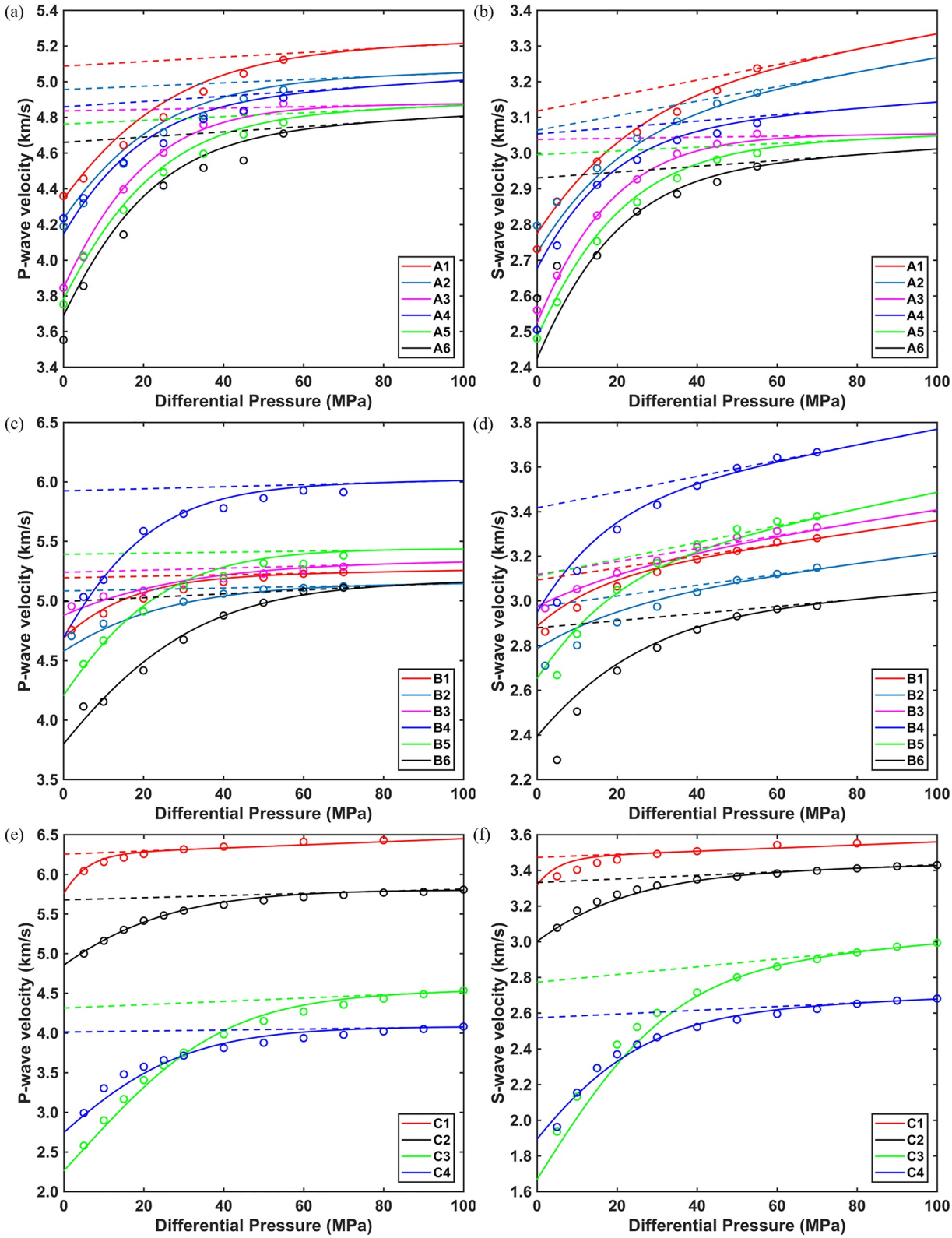

Figure 13. Dry-rock P- and S-wave velocities as a function of the differential pressure for the various samples. The solid line refers to the present model, while the dashed line to the poro-acoustoelasticity model. (a) P-wave velocities of A1–A6; (b) S-wave velocities of A1–A6; (c) P-wave velocities of B1–B6; (d) S-wave velocities of B1–B6; (e) P-wave velocities of C1–C4; (f) S-wave velocities of C1–C4.

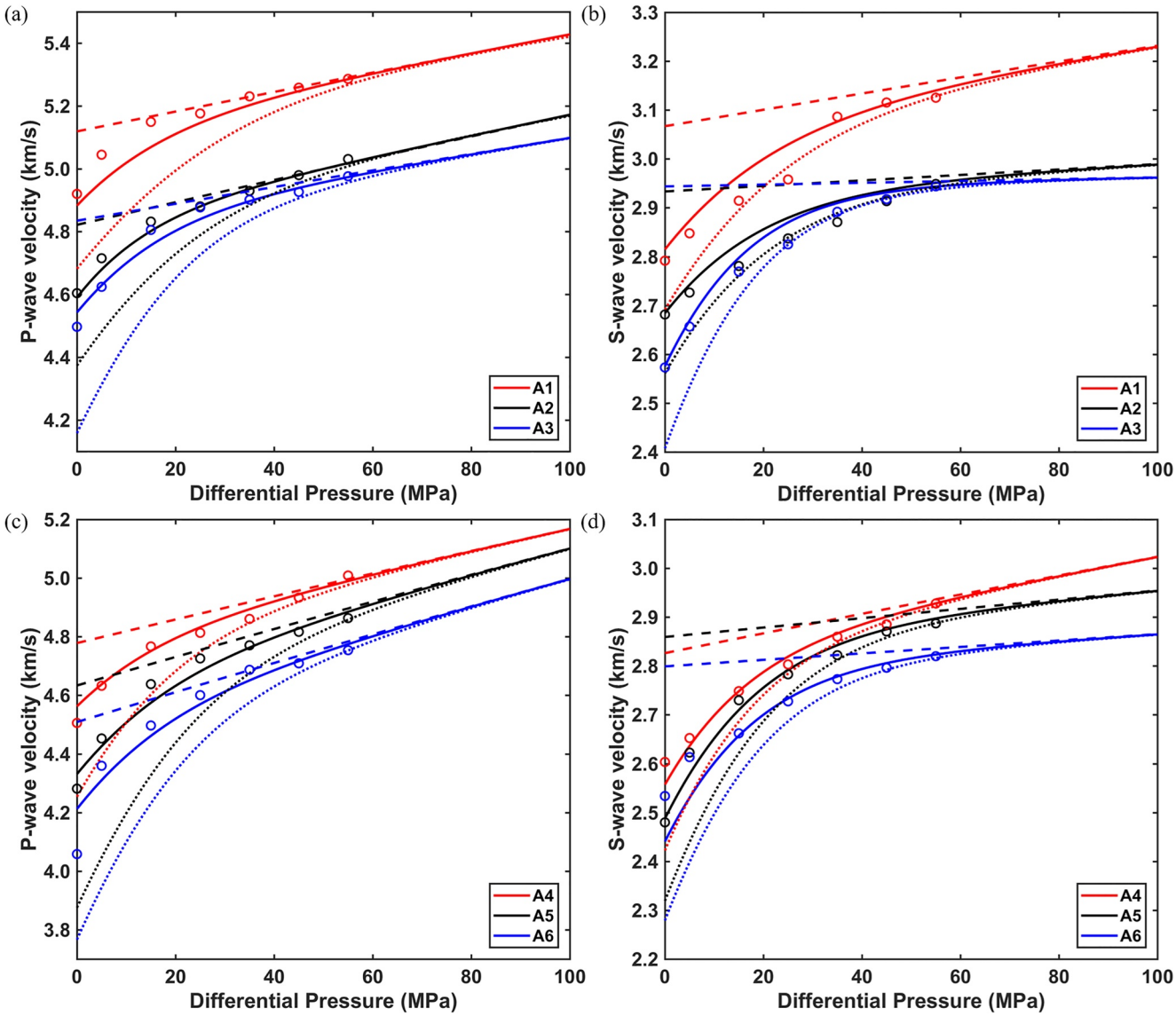

Figure 14. Wet-rock P- and S-wave velocities as a function of the differential pressure for samples A1–A6. The solid line refers to the present model, the dotted line to the double-porosity acoustoelasticity model, and the dashed line to the poro-acoustoelasticity model. (a) P-wave velocities of A1–A3; (b) S-wave velocities of A1–A3; (c) P-wave velocities of A4–A6; (d) S-wave velocities of A4–A6.

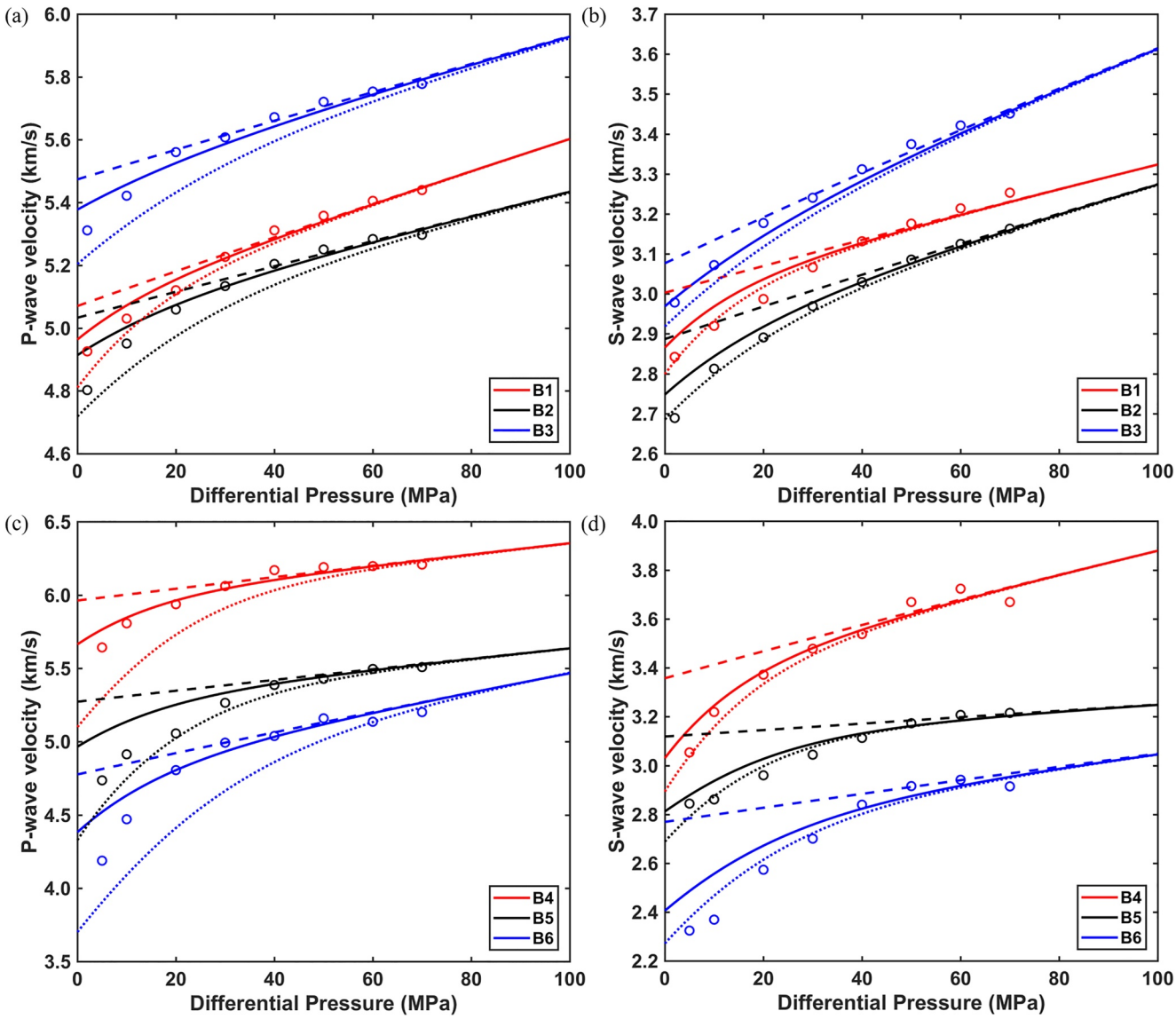

Figure 15. Wet-rock P- and S-wave velocities as a function of the differential pressure for samples B1–B6. The solid line refers to the present model, the dotted line to the double-porosity acoustoelasticity model, and the dashed line to the poro-acoustoelasticity model. (a) P-wave velocities of B1–B3; (b) S-wave velocities of B1–B3; (c) P-wave velocities of B4–B6; (d) S-wave velocities of B4–B6.

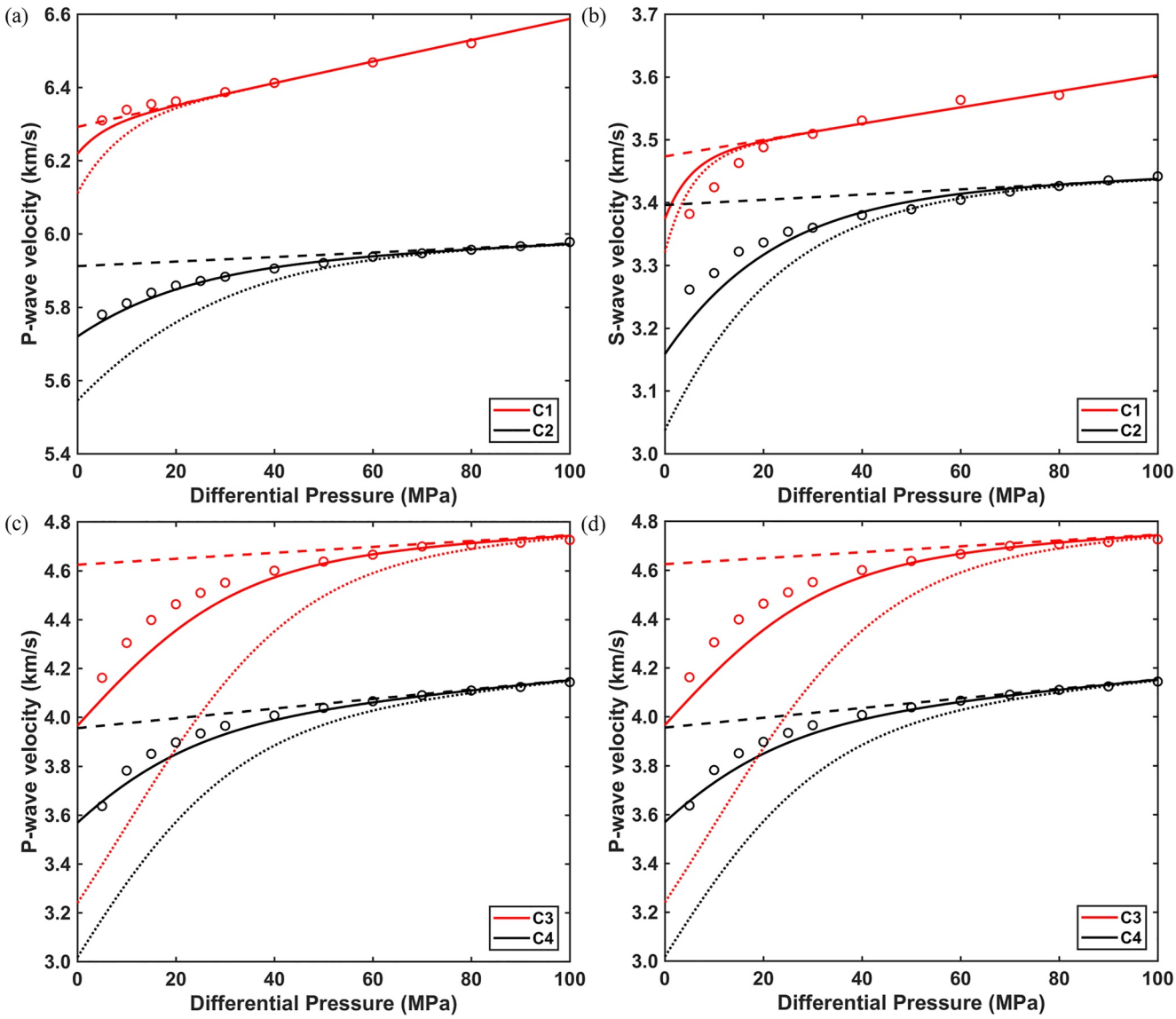

Figure 16. Wet-rock P- and S-wave velocities as a function of the differential pressure for samples C1–C4. The solid line refers to the present model, the dotted line to the double-porosity acoustoelasticity model, and the dashed line to the poro-acoustoelasticity model. (a) P-wave velocities of C1–C2; (b) S-wave velocities of C1–C2; (c) P-wave velocities of C3–C4; (d) S-wave velocities of C3–C4.

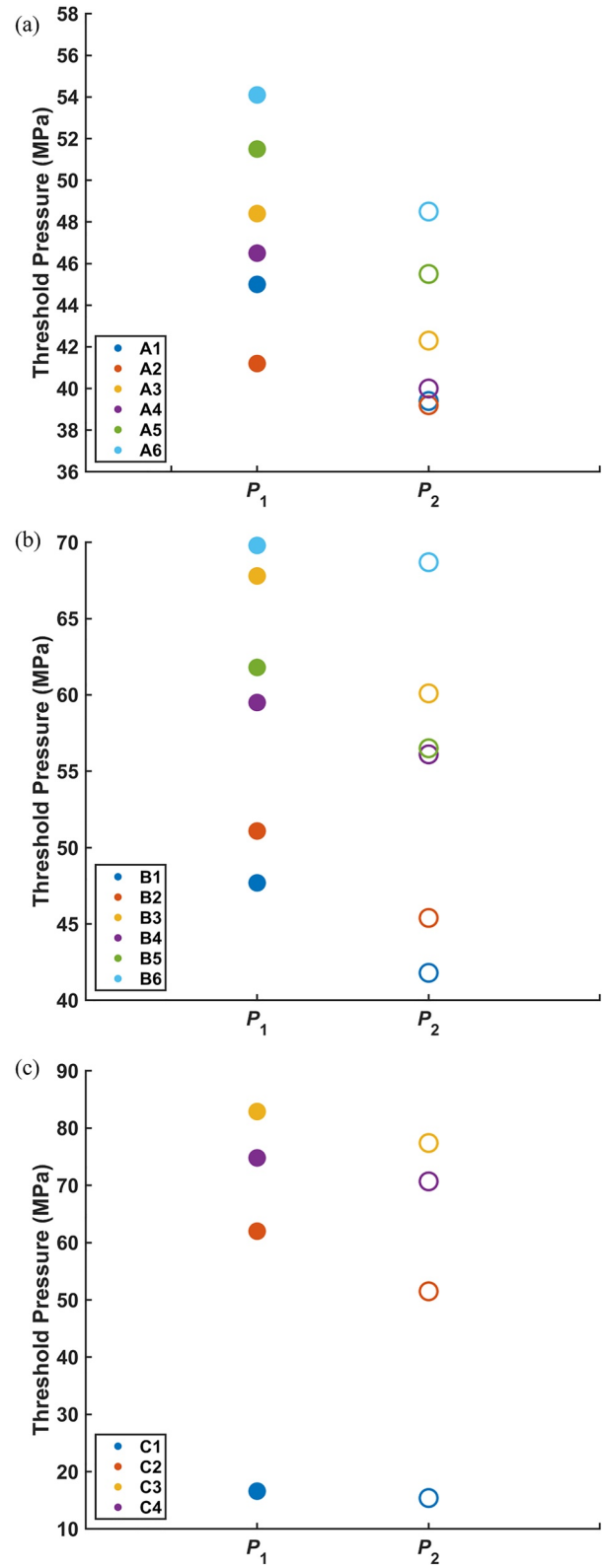

Figure 17. Threshold pressures for samples A1–A6 (a), B1–B6 (b) and C1–C4 (c). The solid circles represent P_1 and the empty ones P_2 .Threshold pressures for Sample.

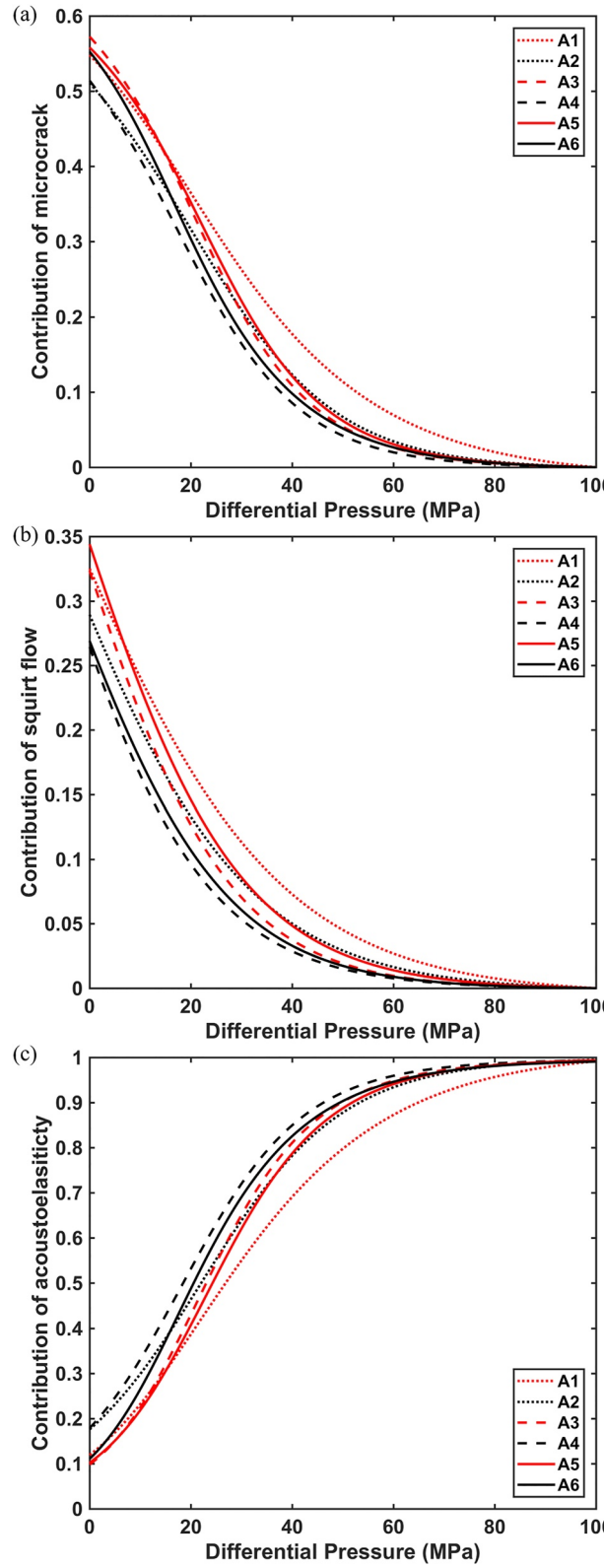

Figure 18. Contributions of crack (a), squirt flow (b) and acoustoelasticity (c) as a function of the differential pressure for samples A1–A6.

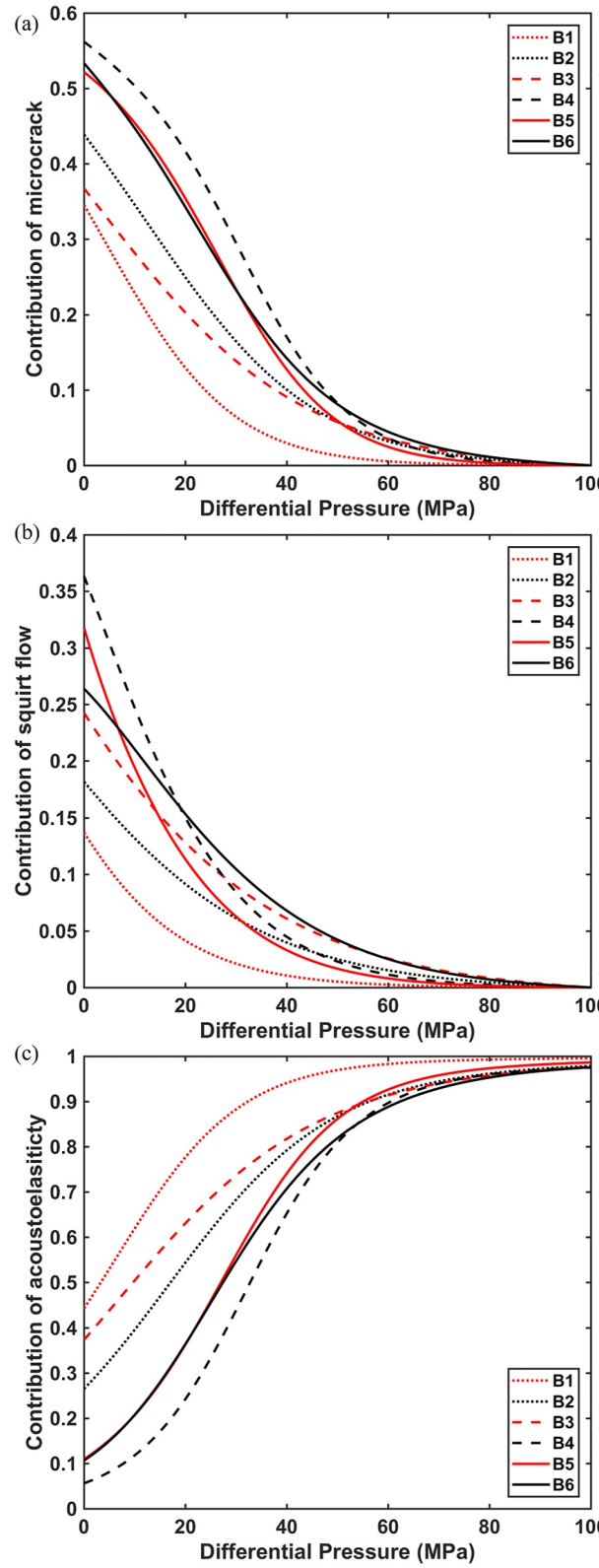

Figure 19. Contributions of crack (a), squirt flow (b) and acoustoelasticity (c) as a function of the differential pressure for samples B1–B6.

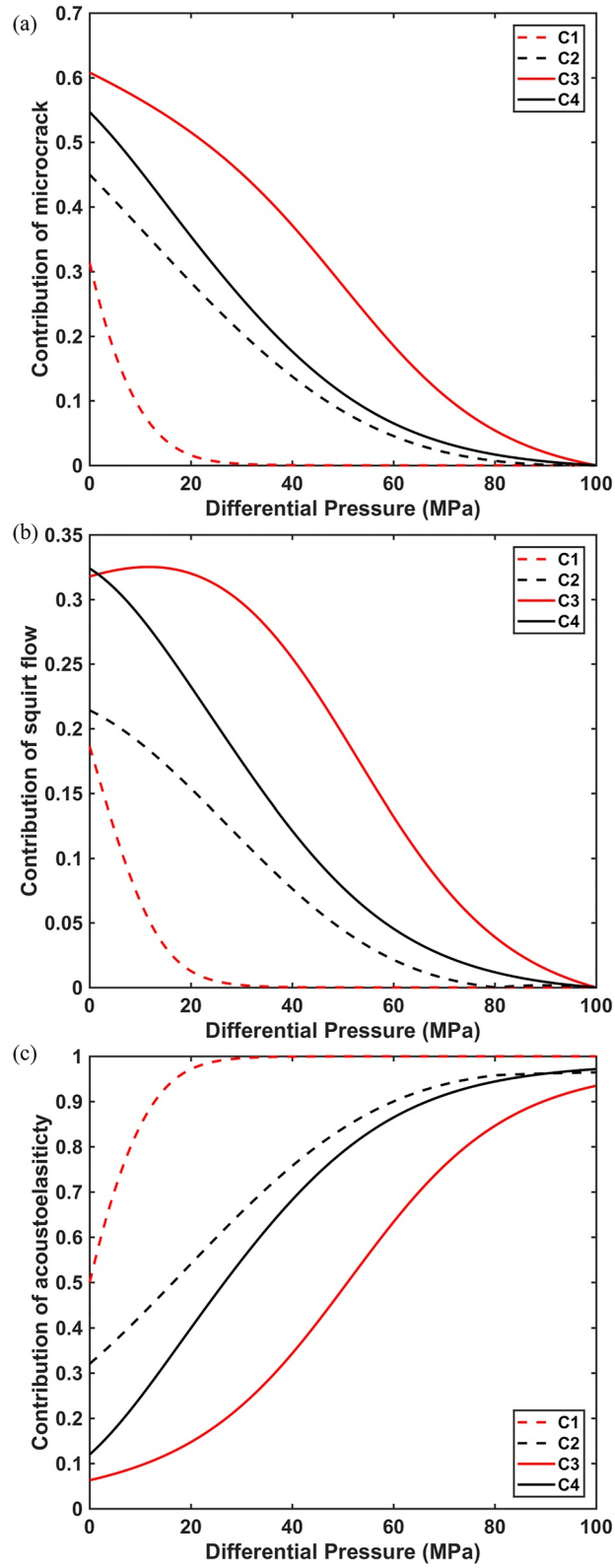

Figure 20. Contribution of crack (a), squirt flow (b) and acoustoelasticity (c) as a function of the differential pressure for samples C1–C4.

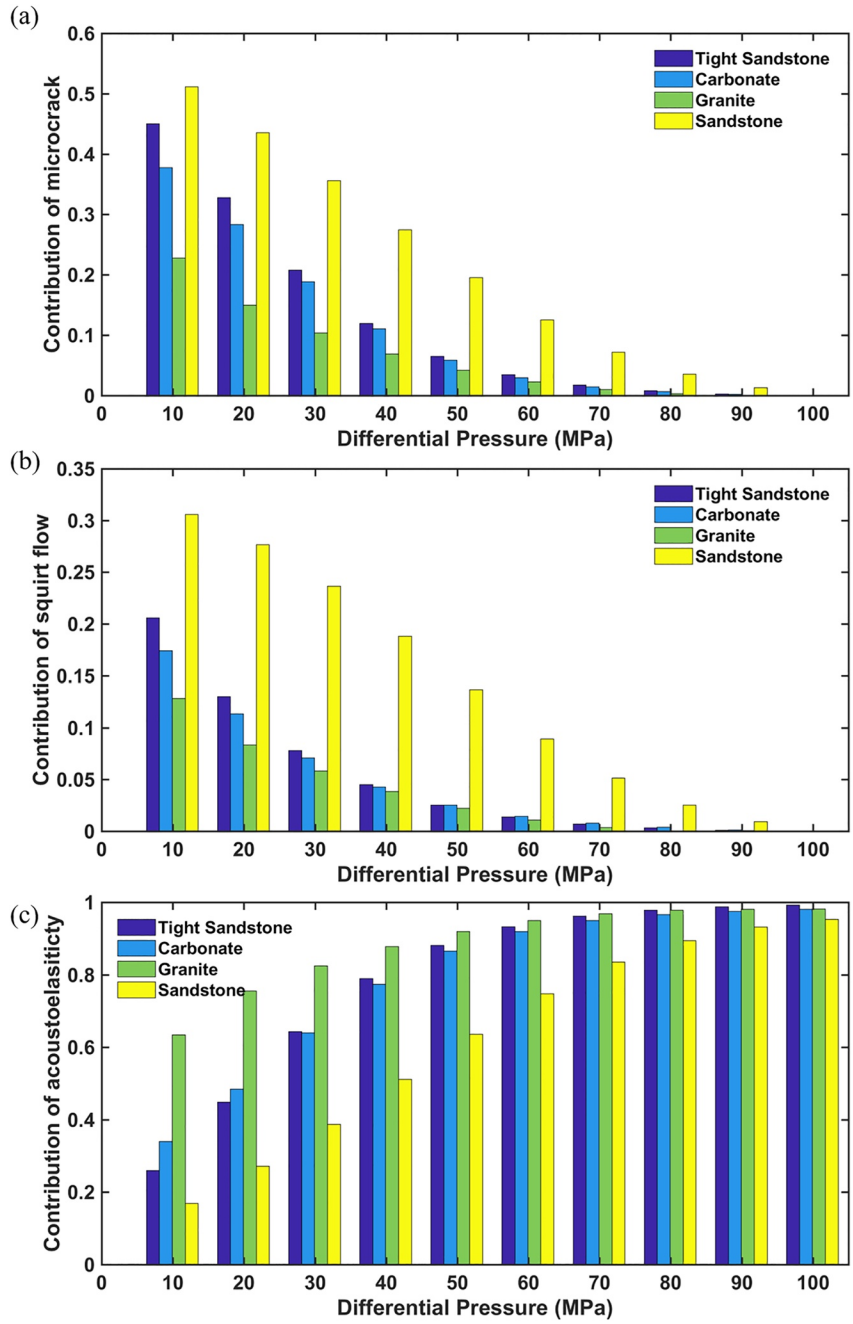

Figure 21. Histogram of the average contribution of crack closure (a), squirt flow (b) and acoustoelasticity (c) as a function of the differential pressure corresponding to the four lithologies.

Appendix A: Shape Factors P and Q

The shape factors P and Q are related to the stiff-pore aspect ratio α and the Poisson ratio υ_g of the grains (David & Zimmerman, 2012; Y. L. Zhang et al., 2019).

$$P = \frac{(1-\upsilon_g)}{6(1-2\upsilon_g)} \cdot \frac{4(1+\upsilon_g)+2\alpha^2(7-2\upsilon_g)-\left[3(1+4\upsilon_g)+12\alpha^2(2-\upsilon_g)\right]g}{2\alpha^2+(1-4\alpha^2)g+(\alpha^2-1)(1+\upsilon_g)g^2} \tag{A1}$$

$$\begin{aligned} Q = {} & \frac{4\left(\alpha^2-1\right)(1-\upsilon_g)}{15\left\{8(\upsilon_g-1)+2\alpha^2(3-4\upsilon_g)+\left[(7-8\upsilon_g)-4\alpha^2(1-2\upsilon_g)\right]g\right\}} \\ & \cdot\left\{\frac{8(1-\upsilon_g)+2\alpha^2(3+4\upsilon_g)+\left[(8\upsilon_g-1)-4\alpha^2(5+2\upsilon_g)\right]g+6\left(\alpha^2-1\right)(1+\upsilon_g)g^2}{2\alpha^2+(1-4\alpha^2)g+(\alpha^2-1)(1+\upsilon_g)g^2}\right. \\ & \left.-3\left[\frac{8(\upsilon_g-1)+2\alpha^2(5-4\upsilon_g)+\left[3(1-2\upsilon_g)+6\alpha^2(\upsilon_g-1)\right]g}{-2\alpha^2+\left[(2-\upsilon_g)+\alpha^2(1+\upsilon_g)\right]g}\right]\right\} \end{aligned} \tag{A2}$$

where $\upsilon_g = \left(3K_g - 2G_g\right) / \left(6K_g + 2G_g\right)$, $g = \begin{cases} \frac{\alpha}{(1-\alpha^2)^{3/2}}\left(\arccos\alpha - \alpha\sqrt{1-\alpha^2}\right) & (\alpha < 1) \\ \frac{\alpha}{(1-\alpha^2)^{3/2}}\left(\alpha\sqrt{1-\alpha^2} - \operatorname{arccosh}\alpha\right) & (\alpha > 1) \end{cases}$.

Appendix B: Batzle and Wang Equations

According to Batzle and Wang (1992), the water density is

$$\begin{aligned} \rho_f = {} & 1 + 10^{-6} \times (-80T - 3.3T^2 + 0.00175T^3 + 489P_p \\ & -2TP + 0.016T^2P_p - 1.3 \times 10^{-5}T^3P_p - 0.333P_p^2 - 0.002TP_p^2) \end{aligned} \tag{B1}$$

where T is the temperature and P_p is the pore pressure.

The wave velocity of water V_f is

$$V_f = \sum_{i=0}^{4}\sum_{j=0}^{3}\omega_{ij}T^iP_p^j \tag{B2}$$

where ω_{ij} are the constants, given in Batzle and Wang (1992).

The modulus of water is

$$k_f = \rho_f \cdot V_f^2, \tag{B3}$$

Data Availability Statement

The experimental data of this study can be accessed at https://doi.org/10.5281/zenodo.6898452.

Acknowledgments
The authors are grateful to the support of the Jiangsu Innovation and Entrepreneurship Plan, Jiangsu Province Science Fund for Distinguished Young Scholars (Grant BK20200021), National Natural Science Foundation of China (Grant 41974123, 42174161), and Postgraduate Research & Practice Innovation Program of Jiangsu Province.

References

Adam, L., Batzle, M., & Brevik, I. (2006). Gassmann fluid substitution and shear modulus variability in carbonates at laboratory seismic and ultrasonic frequencies. *Geophysics*, *71*(6), F173–F183. https://doi.org/10.1190/1.2358494

Ba, J., Carcione, J. M., Cao, H., Yao, F., & Du, Q. (2013). Poro-acoustoelasticity of fluid-saturated rocks. *Geophysical Prospecting*, *61*(3), 599–612. https://doi.org/10.1111/j.1365-2478.2012.01091.x

Ba, J., Carcione, J. M., & Nie, J. X. (2011). Biot-Rayleigh theory of wave propagation in double-porosity media. *Journal of Geophysical Research*, *116*(B6), B06202. https://doi.org/10.1029/2010JB008185

Ba, J., Xu, W., Fu, L. Y., Carcione, J. M., & Zhang, L. (2017). Rock anelasticity due to patchy saturation and fabric heterogeneity: A double double-porosity model of wave propagation. *Journal of Geophysical Research: Solid Earth*, *122*(3), 1949–1976. https://doi.org/10.1002/2016JB013882

Batzle, M. L., Han, D. H., & Hofmann, R. (2006). Fluid mobility and frequency-dependent seismic velocity—Direct measurements. *Geophysics*, *71*(1), N1–N9. https://doi.org/10.1190/1.2159053

Batzle, M. L., & Wang, Z. (1992). Seismic properties of pore fluids. *Geophysics*, *57*(11), 1396–1408. https://doi.org/10.1190/1.1443207
Biot, M. A. (1956). Theory of propagation of elastic waves in a fluid-saturated porous solid. II: Higher frequency range. *Journal of the Acoustical Society of America*, *28*(2), 179–191. https://doi.org/10.1121/1.1908241
Biot, M. A. (1962). Mechanics of deformation and acoustic propagation in porous media. *Journal of Applied Physics*, *33*(4), 1482–1498. https://doi.org/10.1063/1.1728759
Birch, F. (1960). The velocity of compressional waves in rocks to 10 kilobars: 1. *Journal of Geophysical Research*, *65*(4), 1083–1102. https://doi.org/10.1029/JZ065i004p01083
Birch, F. (1961). The velocity of compressional waves in rocks to 10 kilobars: 2. *Journal of Geophysical Research*, *66*(7), 2199–2224. https://doi.org/10.1029/JZ066i007p02199
Brugger, K. (1964). Thermodynamic definition of higher order elastic coefficients. *Physics Review*, *133*(6A), A1611–A1612. https://doi.org/10.1103/PhysRev.133.A1611
Chen, Y., Huang, T. F., & Liu, E. R. (2009). *Rock physics*. China University of Science and Technology Press.
Cheng, C. H., & Toksöz, M. N. (1979). Inversion of seismic velocities for the pore aspect ratio spectrum of a rock. *Journal of Geophysical Research*, *84*(B13), 7533–7543. https://doi.org/10.1029/JB084iB13p07533
Coyner, K. B. (1984). *Effects of stress, pore pressure, and pore fluids on bulk strain, velocity, and permeability in rocks*. Massachusetts Institute of Technology.
David, E. C., Fortin, J., Schubnel, A., Guéguen, N., & Zimmerman, R. W. (2013). Laboratory measurements of low- and high-frequency elastic moduli in Fontainebleau sandstone. *Geophysics*, *78*(5), D367–D377. https://doi.org/10.1190/GEO2013-0070.1
David, E. C., & Zimmerman, R. W. (2012). Pore structure model for elastic wave velocities in fluid-saturated sandstones. *Journal of Geophysical Research*, *117*(B7), B07210. https://doi.org/10.1029/2012JB009195
Deng, J. X., Zhou, H., Wang, H., Zhao, J., & Wang, S. (2015). The influence of pore structure in reservoir sandstone on dispersion properties of elastic waves. *Chinese Journal of Geophysics*, *58*(9), 3389–3400. https://doi.org/10.6038/cjg20150931
Du, S. H., Shi, G. X., Yue, X. J., Kou, G., Zhou, B., & Shi, Y. M. (2019). Imaging-based characterization of perthite in the Upper Triassic Yanchang formation tight sandstone of the Ordos Basin, China. *Acta Geologica Sinica*, *93*(2), 373–385. https://doi.org/10.1111/1755-6724.13768
Dvorkin, J., Mavko, G., & Nur, A. (1995). Squirt flow in fully saturated rocks. *Geophysics*, *60*(1), 97–107. https://doi.org/10.1190/1.1443767
Dvorkin, J., & Nur, A. (1993). Dynamic poroelasticity: A unified model with the squirt and the Biot mechanisms. *Geophysics*, *58*(4), 524–533. https://doi.org/10.1190/1.1443435
Fredrich, J. T., & Wong, T. (1986). Micromechanics of thermally induced cracking in three crustal rocks. *Journal of Geophysical Research*, *91*(B12), 12743–12764. https://doi.org/10.1029/JB091iB12p12743
Fu, B. Y., & Fu, L. Y. (2018). Poro-acoustoelasticity with compliant pores for fluid-saturated rocks. *Geophysics*, *83*(3), WC1–WC14. https://doi.org/10.1190/GEO2017-0423.1
Gassmann, F. (1951). Uber die elastizität poroser Medien. *Vierteljahrsschrift der Naturforschenden Gesellschaft in Zürich*, *96*, 1–23.
Green, R. E. (1973). *Ultrasonic investigation of mechanical properties, treatise on materials science and technology*. Academic Press.
Grinfeld, M. A., & Norris, A. N. (1996). Acoustoelasticity theory and applications for fluid-saturated porous media. *Journal of the Acoustical Society of America*, *100*(3), 1368–1374. https://doi.org/10.1121/1.415983
Guéguen, Y., & Sarout, J. (2009). Crack-induced anisotropy in crustal rocks: Predicted dry and fluid-saturated Thomsen s parameters. *Physics of the Earth and Planetary Interiors*, *172*(1–2), 116–124. https://doi.org/10.1016/j.pepi.2008.05.020
Guéguen, Y., & Sarout, J. (2011). Characteristics of anisotropy and dispersion in cracked medium. *Tectonophysics*, *503*(1–2), 165–172. https://doi.org/10.1016/j.tecto.2010.09.021
Guo, J., & Chen, X. (2022). Pressure dependence of elastic wave velocities of unconsolidated cemented sands. *Geophysics*, *87*(4), MR161–MR175. https://doi.org/10.1190/GEO2021-0595.1
Guo, M., Fu, L., & Ba, J. (2009). Comparison of stress-associated coda attenuation and intrinsic attenuation from ultrasonic measurements. *Geophysical Journal International*, *178*(1), 447–456. https://doi.org/10.1111/j.1365-246X.2009.04159.x
Guo, Y., Liu, J., Yang, H., Liu, Z., Fu, J., Yao, J., et al. (2012). Hydrocarbon accumulation mechanism of low permeable tight lithologic oil fields in the Yanchang Formation, Ordos Basin, China. *Petroleum Exploration and Development*, *39*(4), 447–456. https://doi.org/10.1016/S1876-3804(12)60061-5
Gurevich, B., Makarynska, D., Paula, O. B. D., & Pervukhina, M. (2010). A simple model for squirt-flow dispersion and attenuation in fluid-saturated granular rocks. *Geophysics*, *75*(6), N109–N120. https://doi.org/10.1190/1.3509782
Gurevich, B., Makarynska, D., & Pervukhina, M. (2009). Ultrasonic moduli for fluid-saturated rocks: Mavko-Jizba relations rederived and generalized. *Geophysics*, *74*(4), N25–N30. https://doi.org/10.1190/1.3123802
Han, D., Nur, A., & Morgan, D. (1986). Effects of porosity and clay content on wave velocities in sandstones. *Geophysics*, *51*(11), 2093–2107. https://doi.org/10.1190/1.1442062
Hill, R. (1952). The elastic behaviour of a crystalline aggregate. *Proceedings of the Physical Society*, *65*(5), 349–354. https://doi.org/10.1088/0370-1298/65/5/307
Hughes, D., & Kelly, J. (1953). Second-order elastic deformation of solids. *Physical Review*, *92*(5), 1145–1149. https://doi.org/10.1103/PhysRev.92.1145
Jones, G. L., & Kobett, D. (1963). Interaction of elastic waves in an isotropic solid. *Journal of the Acoustical Society of America*, *35*(1), 5–10. https://doi.org/10.1121/1.1918405
Khaksar, A., Griffiths, C. M., & McCann, C. (1999). Compressional- and shear-wave velocities as a function of confining stress in dry sandstones. *Geophysical Prospecting*, *47*(4), 487–508. https://doi.org/10.1046/j.1365-2478.1999.00146.x
Khazanehdari, J., & Sothcott, J. (2003). Variation in dynamic elastic shear modulus of sandstone upon fluid saturation and substitution. *Geophysics*, *68*(2), 472–481. https://doi.org/10.1190/1.1567213
King, M. S. (1966). Wave velocities in rocks as a function of changes in overburden pressure and pore fluid saturants. *Geophysics*, *31*(1), 50–73. https://doi.org/10.1190/1.1439763
Kravchishin, O. Z., & Chekurin, V. F. (2009). Acoustoelasticity model of inhomogeneously deformed bodies. *Mechanics of Solids*, *44*(5), 781–791. https://doi.org/10.3103/S0025654409050161
Kristinsdóttir, L. H., Flóvenz, O., Arnason, K., Bruhn, D., Milsch, H., Spangenberg, E., & Kulenkampff, J. (2010). Electrical conductivity and P-wave velocity in rock samples from high-temperature Icelandic geothermal fields. *Geothermics*, *39*(1), 94–105. https://doi.org/10.1016/j.geothermics.2009.12.001
Kuster, G. T., & Toksöz, M. N. (1974). Velocity and attenuation of seismic waves in two-phase media: Part I. Theoretical formulations. *Geophysics*, *39*(5), 587–606. https://doi.org/10.1190/1.1440451
Li, Y. Q., Li, S. J., He, D. F., Gao, J., Wang, Y. C., Huang, H. Y., et al. (2020). Middle Triassic tectono-sedimentary development of Sichuan Basin: Insights into the cratonic differentiation. *Geological Journal*, *56*(4), 1858–1878. https://doi.org/10.1002/gj.4033

Liao, J. B., Xi, A. H., Li, Z. Y., Liu, H. Q., Li, X. B., & Rong, W. Y. (2018). Microscopic characterization and formation mechanisms of deep-water sandy-debris-flow and turbidity-current sandstones in a lacustrine basin: A case study in the Yanchang Formation of the Ordos Basin, China. *Petroleum Science*, *15*(1), 28–40. https://doi.org/10.1007/s12182-017-0207-9

Ling, W., Ba, J., Carcione, J. M., & Zhang, L. (2020). Poroacoustoelasticity for rocks with a dual-pore structure. *Geophysics*, *86*(1), 1–43. https://doi.org/10.1190/GEO2020-0314.1

Liu, H., Yang, Y. W., Cheng, B., Cao, Z. C., Wang, S., Jiang, Z. Y., & Yuan, F. F. (2021). Nature of the lower-middle Ordovician reservoir bitumen in the Shunnan area, Tarim Basin, northwestern China. *Journal of Petroleum Science and Engineering*, *209*, 109966. https://doi.org/10.1016/j.petrol.2021.109966

Mavko, G., & Jizba, D. (1991). Estimating grain-scale fluid effects on velocity dispersion in rocks. *Geophysics*, *56*(12), 1940–1949. https://doi.org/10.1190/1.1443005

Mavko, G., Mukerji, T., & Dvorkin, J. (2009). *The Rock Physics Handbook: Tools for seismic analysis in porous media*. Cambridge University Press.

Mavko, G., & Nolen-Hoeksema, R. C. (1994). Estimating seismic velocities at ultrasonic frequencies in partially saturated rocks. *Geophysics*, *59*(2), 252–258. https://doi.org/10.1190/1.1443587

Meegan, G. D., Johnson, P. A., Guyer, R. A., & McCall, K. R. (1993). Observations on nonlinear elastic wave behavior in sandstone. *Journal of the Acoustical Society of America*, *94*(6), 3387–3391. https://doi.org/10.1121/1.407191

Mori, T., & Tanaka, K. (1973). Average stress in matrix and average elastic energy of materials with misfitting inclusions. *Acta Metallurgica*, *21*(5), 571–574. https://doi.org/10.1016/0001-6160(73)90064-3

Murphy, W. F., Winkler, K. W., & Kleinberg, R. L. (1986). Acoustic relaxation in sedimentary rocks: Dependence on grain contacts and fluid saturation. *Geophysics*, *51*(3), 757–766. https://doi.org/10.1190/1.1442128

Njiekak, G., & Schmitt, D. (2019). Effective stress coefficient for seismic velocities in carbonate rocks: Effects of pore characteristics and fluid types. *Pure and Applied Geophysics*, *176*(4), 1467–1485. https://doi.org/10.1007/s00024-018-2045-0

Nur, A. (1971). Effects of stress on velocity anisotropy in rocks with cracks. *Journal of Geophysical Research*, *76*(8), 2022–2034. https://doi.org/10.1029/JB076i008p02022

Nur, A., & Simmons, G. (1969). Stress-induced velocity anisotropy in rock: An experimental study. *Journal of Geophysical Research*, *74*(27), 6667–6674. https://doi.org/10.1029/JB074i027p06667

Pecorari, C. (1997). Acoustoelasticity in cracked solids. *Geophysical Journal International*, *129*(1), 169–175. https://doi.org/10.1111/j.1365-246X.1997.tb00946.x

Pham, N. H., Carcione, J. M., Helle, H. B., & Ursin, B. (2002). Wave velocities and attenuation of shaley sandstones as a function of pore pressure and partial saturation. *Geophysical Prospecting*, *50*(6), 615–627. https://doi.org/10.1046/j.1365-2478.2002.00343.x

Pimienta, L., Fortin, J., & Guéguen, Y. (2015). Experimental study of Young's modulus dispersion and attenuation in fully saturated sandstones. *Geophysics*, *80*(5), L57–L72. https://doi.org/10.1190/GEO2014-0532.1

Pimienta, L., Fortin, J., & Guéguen, Y. (2016). Effect of fluids and frequencies on Poisson's ratio of sandstone samples. *Geophysics*, *81*(2), D183–D195. https://doi.org/10.1190/GEO2015-0310.1

Quintal, B., Steeb, H., Frehner, M., Schmalholz, S. M., & Saenger, E. H. (2012). Pore fluid effects on S-wave attenuation caused by wave-induced fluid flow. *Geophysics*, *77*(3), L13–L23. https://doi.org/10.1190/geo2011-0233.1

Regnet, J. B., David, C., Robion, P., & Menendez, B. (2019). Microstructures and physical properties in carbonate rocks: A comprehensive review. *Marine and Petroleum Geology*, *103*, 366–376. https://doi.org/10.1016/j.marpetgeo.2019.02.022

Reuss, A. (1929). Calculation of the flow limits of mixed crystals on the basis of the plasticity of monocrystals. *Zeitschrift fur Angewandte Mathematik und Mechanik*, *9*(1), 49–58. https://doi.org/10.1002/zamm.19290090104

Saenger, E. H., Kruger, O. S., & Shapiro, S. A. (2004). Effective elastic properties of randomly fractured soils: 3D numerical experiments. *Geophysical Prospecting*, *52*(3), 183–195. https://doi.org/10.1111/j.1365-2478.2004.00407.x

Sarout, J. (2012). Impact of pore space topology on permeability, cut-off frequencies and validity of wave propagation theories. *Geophysical Journal International*, *189*(1), 481–492. https://doi.org/10.1111/j.1365-246X.2011.05329.x

Shapiro, S. A. (2003). Elastic piezosensitivity of porous and fractured rocks. *Geophysics*, *68*(2), 482–486. https://doi.org/10.1190/1.1567215

Shen, H., Li, X., Li, Q., & Wang, H. (2020). A method to model the effect of pre-existing cracks on P-wave velocity in rocks. *Journal of Rock Mechanics and Geotechnical Engineering*, *12*(3), 493–506. https://doi.org/10.1016/j.jrmge.2019.10.001

Simmons, G. (1964). Velocity of shear waves in rocks to 10 kilobars. *Journal of Geophysical Research*, *69*(6), 1123–1130. https://doi.org/10.1029/JZ069i006p01123

Sinha, B. K., & Kostek, S. (1996). Stress-induced azimuthal anisotropy in borehole flexural waves. *Geophysics*, *61*(6), 1899–1907. https://doi.org/10.1190/1.1444105

Sinha, B. K., Kostek, S., & Norris, A. N. (1995). Stoneley and flexural modes in pressurized boreholes. *Journal of Geophysical Research*, *100*(B11), 22375–22381. https://doi.org/10.1029/95JB02504

Smith, T., Sondergeld, C., & Tinni, A. O. (2010). Microstructural controls on electric and acoustic properties in tight gas sandstones; some empirical data and observations. *The Leading Edge*, *29*(12), 1470–1474. https://doi.org/10.1190/1.3525362

Sun, Y. Y., & Gurevich, B. (2020). Modeling the effect of pressure on the moduli dispersion in fluid-saturated rocks. *Journal of Geophysical Research: Solid Earth*, *125*(8), e2019JB019297. https://doi.org/10.1029/2019JB019297

Tran, D. T., Rai, C. S., & Sondergeld, C. H. (2008). Changes in crack aspect-ratio concentration from heat treatment: A comparison between velocity inversion and experimental data. *Geophysics*, *71*(4), E123–E132. https://doi.org/10.1190/1.2928848

Tutuncu, A. N., & Sharma, M. M. (1992). The influence of fluids on grain contact stiffness and frame moduli in sedimentary rocks. *Geophysics*, *57*(12), 1571–1582. https://doi.org/10.1190/1.1443225

Vernik, L., & Kachanov, M. (2010). Modeling elastic properties of siliciclastic rocks. *Geophysics*, *75*(6), E171–E182. https://doi.org/10.1190/1.3494031

Voigt, W. (1910). *Lehrbuch der Kirstallphysik*. Teubner.

Walsh, J. B. (1965). The effect of cracks on the compressibility of rock. *Journal of Geophysical Research*, *70*(2), 381–389. https://doi.org/10.1029/JZ070i002p00381

Wang, H. F., Bonner, B. P., Carlson, S. R., Kowallis, B. J., & Heard, H. C. (1989). Thermal stress cracking in granite. *Journal of Geophysical Research*, *94*(B2), 1745–1758. https://doi.org/10.1029/JB094iB02p01745

Winkler, K. W., & Liu, X. (1996). Measurements of third-order elastic constants in rocks. *Journal of the Acoustical Society of America*, *100*(3), 1392–1398. https://doi.org/10.1121/1.415986

Winkler, K. W., & McGowan, L. (2004). Nonlinear acoustoelastic constants of dry and saturated rocks. *Journal of Geophysical Research*, *109*(B10), B10204. https://doi.org/10.1029/2004JB003262

Wyllie, M. R. J., Gregory, A. R., & Gardner, G. H. F. (1958). An experimental investigation of factors affecting elastic wave velocities in porous media. *Geophysics*, *23*(3), 459–493. https://doi.org/10.1190/1.1438493

Yang, H., & Zhang, W. Z. (2005). Leading effect of the seventh member high quality source rock of Yanchang Formation in Ordos Basin during the enrichment of low-penetrating oil–gas accumulation: Geology and geochemistry. *Geochimica*, *34*(2), 147–154. https://doi.org/10.19700/j.0379-1726.2005.02.007

Zaitsev, V. Y., Radostin, A. V., Pasternak, E., & Dyskin, A. (2017). Extracting shear and normal compliances of crack-like defects from pressure dependences of elastic-wave velocities. *International Journal of Rock Mechanics and Mining Sciences*, *97*, 122–133. https://doi.org/10.1016/j.ijrmms.2017.04.009

Zhang, L., Ba, J., & Carcione, J. M. (2021). Wave propagation in infinituple-porosity media. *Journal of Geophysical Research: Solid Earth*, *126*(4), e2020JB021266. https://doi.org/10.1029/2020JB021266

Zhang, L., Ba, J., Carcione, J. M., & Wu, C. (2022). Seismic wave propagation in partially saturated rocks with a fractal distribution of fluid-patch size. *Journal of Geophysical Research: Solid Earth*, *127*(2), e2021JB023809. https://doi.org/10.1029/2021JB023809

Zhang, L., Ba, J., Fu, L. Y., Carcione, J. M., & Cao, C. H. (2019). Estimation of pore microstructure by using the static and dynamic moduli. *International Journal of Rock Mechanics and Mining Sciences*, *113*, 24–30. https://doi.org/10.1016/j.ijrmms.2018.11.005

Zhang, Y. L., Bao, Z. D., Zhao, Y., Jiang, L., & Gong, F. H. (2017). Diagenesis and its controls on reservoir properties and hydrocarbon potential in tight sandstone: A case study from the upper Triassic Chang 7 oil group of Yanchang Formation, Ordos Basin, China. *Arabian Journal of Geosciences*, *10*(11), 234. https://doi.org/10.1007/s12517-017-3023-z

Zhao, J. H., Zhao, R., Wu, Y. S., Liu, T. J., Cui, X. M., & Guo, K. Z. (2018). The origin and distribution of Ordovician Yingshan dolomite on the northern slope of Tazhong area in Tarim Basin. *Carbonates and Evaporites*, *34*(3), 507–523. https://doi.org/10.1007/s13146-018-0479-1

Zimmerman, R. W. (1991). *Compressibility of sandstones*. Elsevier.